

# RADIAL TRANSPORT OF LARGE-SCALE MAGNETIC FIELDS IN ACCRETION DISKS. I. STEADY SOLUTIONS AND AN UPPER LIMIT ON THE VERTICAL FIELD STRENGTH

SATOSHI OKUZUMI<sup>1</sup>, TAKU TAKEUCHI<sup>1</sup>, AND TAKAYUKI MUTO<sup>2</sup>

<sup>1</sup>Department of Earth and Planetary Sciences, Tokyo Institute of Technology, Meguro-ku, Tokyo 152-8551, Japan; okuzumi@geo.titech.ac.jp

<sup>2</sup>Division of Liberal Arts, Kogakuin University, 1-24-2, Nishi-Shinjuku, Shinjuku-ku, Tokyo 163-8677, Japan

*ApJ, in press*

## ABSTRACT

Large-scale magnetic fields are key ingredients of magnetically driven disk accretion. We study how large-scale poloidal fields evolve in accretion disks, with the primary aim of quantifying the viability of magnetic accretion mechanisms in protoplanetary disks. We employ a kinematic mean-field model for poloidal field transport and focus on steady states where inward advection of a field balances with outward diffusion due to effective resistivities. We analytically derive the steady-state radial distribution of poloidal fields in highly conducting accretion disks. The analytic solution reveals an upper limit on the strength of large-scale vertical fields attainable in steady states. Any excess poloidal field will diffuse away within a finite time, and we demonstrate this with time-dependent numerical calculations of the mean-field equations. We apply this upper limit to large-scale vertical fields threading protoplanetary disks. We find that the maximum attainable strength is about 0.1 G at 1 AU, and about 1 mG at 10 AU from the central star. When combined with recent magnetic accretion models, the maximum field strength translates into the maximum steady-state accretion rate of  $\sim 10^{-7} M_{\odot} \text{ yr}^{-1}$ , in agreement with observations. We also find that the maximum field strength is  $\sim 1$  kG at the surface of the central star provided that the disk extends down to the stellar surface. This implies that any excess stellar poloidal field of strength  $\gtrsim$  kG can be transported to the surrounding disk. This might in part resolve the magnetic flux problem in star formation.

*Keywords:* accretion, accretion disks – magnetic fields – magnetohydrodynamics (MHD) – planets and satellites: formation – protoplanetary disks – stars: formation

## 1. INTRODUCTION

Young stars host gaseous accretion disks called protoplanetary disks. They are a by-product of star formation from a molecular cloud. Observed protoplanetary disks (of age  $\sim 1$  Myr) are characterized by an outer radius of  $\sim 100$  AU (Kitamura et al. 2002; Andrews et al. 2009) and an accretion rate of  $\sim 10^{-9}$ – $10^{-7} M_{\odot} \text{ yr}^{-1}$  (Hartmann et al. 1998; Calvet et al. 2004; Sicilia-Aguilar et al. 2005). To understand how the disks form, evolve, and dissipate with time is essential for understanding how planets form there.

It is widely accepted that large-scale magnetic fields play key roles in disk evolution. They not only drive turbulence via magnetorotational instability (MRI; Balbus & Hawley 1991, 1998) but also accelerate winds and outflows via the magnetocentrifugal mechanism (Blandford & Payne 1982; Spruit 1996). Both mechanisms transport the angular momentum of disks, leading to accretion of disk material. In addition, turbulence driven by MRI has many effects on the motion of solid bodies in the disks and hence on planet formation. The effects include aerodynamical stirring of small dust particles (e.g., Carballido et al. 2005; Turner et al. 2006; Fromang & Papaloizou 2006; Johansen et al. 2006; Okuzumi & Hirose 2011, 2012) and gravitational stirring of larger solid bodies (e.g., Laughlin et al. 2004; Nelson & Papaloizou 2004; Nelson 2005; Yang et al. 2009, 2012; Gressel et al. 2011, 2012; Okuzumi & Ormel 2013; Ormel & Okuzumi 2013).

A key parameter of these accretion mechanisms is the strength of the poloidal field threading the disk. Early local-box MHD simulations by Hawley et al. (1995) already suggested a positive dependence of the MRI-driven accretion stress on the large-scale field strength (see also

Sano et al. 2004; Pessah et al. 2007). More realistic simulations including vertical gas stratification (Suzuki et al. 2010; Bai & Stone 2013a), ohmic diffusion (Okuzumi & Hirose 2011; Gressel et al. 2012), and/or ambipolar diffusion (Simon et al. 2013a,b) have not changed this basic picture in the sense that the vertical average of the accretion stress increases with the strength of the net (large-scale) vertical field. The accretion stress produced by magnetocentrifugal winds also exhibits a positive dependence on the net poloidal field strength (Simon et al. 2013b; Bai & Stone 2013a,b; Bai 2013). Accretion disk models taking into account these dependences predict that the net vertical field strength determines the fate of disk evolution (Suzuki et al. 2010; Armitage et al. 2013). Therefore, in order to understand the evolution of accretion disks, one needs to understand the evolution of poloidal fields threading the disks.

Radial transport of a large-scale poloidal field is a long-standing issue in the theory of accretion disks. Early studies argued that accretion disks would advect weak interstellar magnetic field inward and build up a strong field at the center of the disks (Bisnovatyi-Kogan & Ruzmaikin 1974; Lovelace 1976). However, this picture was later confronted with an issue raised by van Ballegoijen (1989) and Lubow et al. (1994a, henceforth LPP94a). They argued that if turbulence is the source of disk accretion, then large-scale fields would diffuse away faster than they are advected inward. Their argument is as follows. Consider a turbulent disk and assume that the turbulence acts as an effective viscosity  $\nu_{\text{turb}}$  on disk matter and as an effective resistivity (diffusivity)  $\eta_{\text{turb}}$  on large-scale magnetic fields. Then, an order-of-magnitude estimate of the mean-field induction equation shows that significant field dragging occurs only when  $\mathcal{D} \equiv (\text{Pm}_{\text{turb}} h)^{-1}$  is less than unity, where  $h$  is the disk's aspect ratio ( $\ll 1$  for thin disks)

and  $\text{Pm}_{\text{turb}} = \nu_{\text{turb}}/\eta_{\text{turb}}$  is the turbulent magnetic Prandtl number. The large factor  $h^{-1}$  in  $\mathcal{D}$  comes from the fact that even a slightly bent poloidal field can lead to a large electric current in a thin accretion disk. One finds that if  $\text{Pm}_{\text{turb}} \sim 1$ , as is the case for MRI turbulence (Guan & Gammie 2009; Lesur & Longaretti 2009; Fromang & Stone 2009), then the above criterion is violated, i.e., diffusion would prevent advection of the field. This has been invoked as a challenge to the viability of magnetically driven jets and winds. This also implies that MRI turbulence would saturate at a low level. For protoplanetary disks, the level might be too low to be consistent with observations (Bai & Stone 2013b; Simon et al. 2013a).

However, recent studies suggest that poloidal fields are more likely to be advected than previously thought. Spruit & Uzdensky (2005) point out that turbulent diffusion is reduced if the magnetic flux passes through the disk in concentrated patches. Turbulent diffusion can also be prevented if the disk has highly conductive (non-turbulent) surface layers (Bisnovatyi-Kogan & Lovelace 2007, 2012; Rothstein & Lovelace 2008; Lovelace et al. 2009). Guilet & Ogilvie (2012, 2013) point out that the advection of magnetic flux can be significantly faster than that of mass owing to fast radial velocities in the low-density regions away from the midplane (Takeuchi & Lin 2002).

Efficient advection of magnetic flux is also suggested by a number of global MHD simulations (Igumenshchev et al. 2003; Beckwith et al. 2009; Tchekhovskoy et al. 2011; Suzuki & Inutsuka 2014), some of which (Beckwith et al. 2009; Suzuki & Inutsuka 2014) indicate that the advection indeed takes place at large distances from the midplane. Taken together, these results suggest that poloidal fields can be efficiently dragged inward (i.e.,  $\mathcal{D}$  can be  $< 1$ ) in a realistic accretion disk.

These recent studies motivate us to ask the following questions. Assuming that advection of a poloidal field is indeed efficient, how will the radial distribution of the poloidal field evolve with time? Can we constrain the range of the poloidal field strength for such a conducting accretion disk? What are the implications for magnetically driven evolution of accretion disks such as protoplanetary disks? Aiming at addressing these questions, we revisit global transport of large-scale magnetic fields with the assumption that poloidal fields can be efficiently dragged inward in accretion disks. As a first step of this project, we here focus on steady states where inward advection of a magnetic flux balances with outward diffusion. We employ the kinematic mean-field formalism of LPP94a and analytically derive the steady-state distribution of a poloidal field for highly conducting accretion disks. We find that there exists an upper limit on the vertical field strength for a given distance from the central star. When combined with recent models for MRI and wind-driven accretion, this upper limit suggests that magnetically driven accretion does not produce an accretion rate higher than  $\sim 10^{-7} M_{\odot} \text{ yr}^{-1}$  as long as the magnetic field configuration reaches a steady state. A companion paper addresses non-steady field transport in evolving viscous accretion disks (Takeuchi & Okuzumi 2014).

The plan of the paper is as follows. In Section 2 we introduce the model to describe radial transport of magnetic fields, and derive the condition to be satisfied in steady states. In Section 3 we analytically derive the steady-state equations as well as the upper limit on the vertical field strength. Section 4 compares the analytic solution with time-dependent numeri-

cal solutions. In Section 5 we apply our result to protoplanetary systems and discuss its astrophysical implications. Section 6 is devoted to a summary.

## 2. MODEL

In this study, we adopt a mean-field model for large-scale poloidal fields developed by LPP94a (see Figure 1 for a schematic illustration). We take a cylindrical coordinate system  $(r, \phi, z)$  with  $r = 0$  at the disk center and  $z = 0$  on the disk midplane. We denote the large-scale averages of the magnetic field strength and neutral gas velocity as  $\mathbf{B}$  and  $\mathbf{u}$ , respectively. The adopted model is kinematic in the sense that  $\mathbf{u}$  is given as a prescribed function. Any small-scale (or turbulent) motion in the disk is treated as a macroscopic magnetic diffusivity, which will also be given as a prescribed quantity (see Section 2.1 below). In principle, one can evolve  $\mathbf{B}$  and  $\mathbf{u}$  in a self-consistent way by solving dynamical equations or adopting any empirical relation between  $\mathbf{B}$  and  $\mathbf{u}$  (see Agapitou & Papaloizou 1996), but we defer this to future work.

We assume that both  $\mathbf{B}$  and  $\mathbf{u}$  are axisymmetric, or that these quantities are already averaged in the azimuthal direction. Therefore, we do not explicitly treat transport of strongly magnetized patches as considered by Spruit & Uzdensky (2005). We neglect conversion of toroidal into poloidal fields by turbulence (the so-called  $\alpha$  dynamo), though such effects do exist in MRI-driven turbulence (e.g., Brandenburg et al. 1995; Davis et al. 2010; Gressel 2010; Simon et al. 2011; Flock et al. 2012a,b). With this assumption together with axisymmetry, the toroidal field  $B_{\phi}$  does not enter the induction equation for the poloidal field. For this reason, we will treat the disk field as purely poloidal.

The accretion disk is assumed to be geometrically thin with half thickness  $H \ll r$ . The large-scale electric current  $\mathbf{J} = (c/4\pi)\nabla \times \mathbf{B}$  is purely toroidal since  $\mathbf{B}$  is axisymmetric and poloidal. We assume that the toroidal current is well confined to the disk ( $|z| < H$ ). The magnetic field exterior to the disk is therefore a potential field.

We express the poloidal field in terms of a flux function  $\psi$  defined as  $\mathbf{B} = \nabla \times (\psi \mathbf{e}_{\phi}/r)$ . By axisymmetry, the radial and azimuthal components of the field are written as

$$B_r = -\frac{1}{r} \frac{\partial \psi}{\partial z}, \quad (1)$$

$$B_z = \frac{1}{r} \frac{\partial \psi}{\partial r}. \quad (2)$$

The flux function is proportional to the magnetic flux  $\Phi(r)$  passing through the disk interior to  $r$ , i.e.,

$$\Phi(r) = 2\pi \int_0^r B_z(r', 0) r' dr' = 2\pi \psi(r, 0). \quad (3)$$

### 2.1. Disk-field Equation

The time evolution of a poloidal flux distribution is determined by the mean-field induction equation. In terms of  $\psi$ , this can be written as (see Equation (10) of LPP94a)

$$\frac{\partial \psi}{\partial t} = -u_r \frac{\partial \psi}{\partial r} - \frac{4\pi r \eta}{c} J_{\phi}, \quad (4)$$

where  $u_r(r, z)$  is the mean radial velocity,  $\eta(r, z)$  is the magnetic diffusivity (resistivity), and

$$J_{\phi} = \frac{c}{4\pi} (\nabla \times \mathbf{B})_{\phi} = \frac{c}{4\pi} \left( \frac{\partial B_r}{\partial z} - \frac{\partial B_z}{\partial r} \right) \quad (5)$$

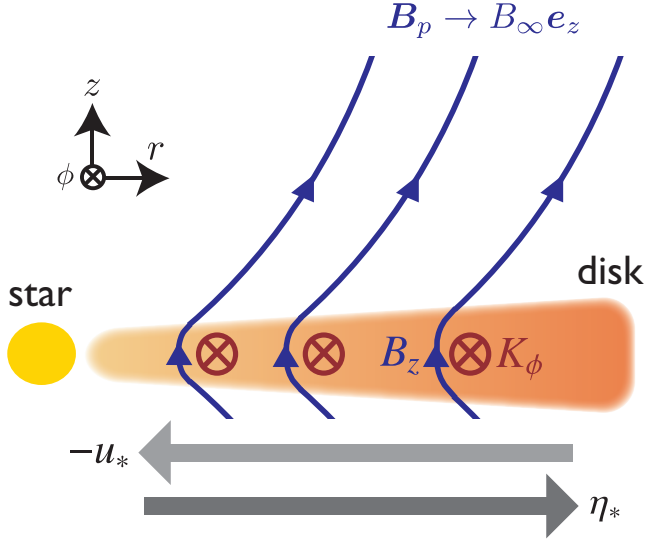


**Figure 1.** Schematic illustration of the mean-field model adopted in this study. The disk is assumed to be threaded by a large-scale poloidal field  $\mathbf{B}_p = B_r \mathbf{e}_r + B_z \mathbf{e}_z$  (solid curves; note that the field lines below the disk are omitted). The field connects to a uniform field  $B_\infty \mathbf{e}_z$  at infinity. The flux is advected inward at some averaged speed  $|u_*|$  (Equation (8)) and is diffused outward by some effective resistivity  $\eta_*$  (Equation (9)). The surface density of the toroidal current,  $K_\phi$ , is related to the flux distribution on the disk by Biot–Savart’s law (Equation (12)).

is the toroidal component of the mean electric current. In the framework of the mean-field theory, the diffusivity in Equation (4) may be interpreted as the sum of the molecular (microscopic) diffusivity  $\eta_{\text{mol}}$  and the turbulent (macroscopic) diffusivity  $\eta_{\text{turb}}$ . Formally, Equation (4) neglects the Hall term and ambipolar diffusion. However, if  $\mathbf{B}$  is poloidal and  $\mathbf{J}$  is toroidal as envisaged here, then ambipolar diffusion is identical to ohmic diffusion (because  $\mathbf{J} \perp \mathbf{B}$ ), and the toroidal component of the Hall term vanishes (because the Hall term  $\propto \mathbf{J} \times \mathbf{B}$ ).<sup>1</sup> In this case, the non-ohmic effects only amount to adding the ambipolar diffusivity to  $\eta$  in Equation (4) (the so-called Pedersen diffusivity; see, e.g., Wardle & Salmeron 2012).

For a geometrically thin disk, where  $\psi$  is approximately independent of  $z$ , one can reduce Equation (4) to a one-dimensional equation with any vertical averaging (LPP94a, Ogilvie & Livio 2001). In this study, we follow Ogilvie & Livio (2001) and average the equation after weighting the “conductivity”  $\eta^{-1}$ . Dividing Equation (4) by  $\eta$  and integrating it over  $-H < z < H$ , we obtain the conductivity-weighted average of the induction equation (see Equation (9) of Ogilvie & Livio 2001)

$$\frac{\partial \psi}{\partial t} = -u_* \frac{\partial \psi}{\partial r} - \frac{2\pi r \eta_*}{cH} K_\phi, \quad (6)$$

where

$$K_\phi(r) \equiv \int_{-H}^H J_\phi(r, z) dz \quad (7)$$

<sup>1</sup> We note that this argument holds only when the cross-correlations of small-scale quantities arising from the non-ohmic terms are negligible. For example, see Equation (24) of Kunz & Lesur (2013) for a mean-field equation including a cross-correlation from the Hall term. We also note that accretion disks can in fact have a strong toroidal field owing to the orbital shear (Turner & Sano 2008).

is the toroidal component of the surface current density,

$$u_*(r) \equiv \frac{\eta_*}{2H} \int_{-H}^H \frac{u_r(r, z)}{\eta(r, z)} dz \quad (8)$$

is the conductivity-weighted average of the radial gas velocity, and

$$\frac{1}{\eta_*(r)} \equiv \frac{1}{2H} \int_{-H}^H \frac{dz}{\eta(r, z)} \quad (9)$$

is the height average of the conductivity. An advantage of the conductivity-weighted average is that the resulting induction equation (Equation (6)) does not involve the vertical distribution of  $J_\phi$ . The vertically integrated current  $K_\phi$  is sufficient, and this can be determined from the field configuration exterior to the disk (Ogilvie & Livio 2001; see also Section 2.2 below). Furthermore, it naturally accounts for the fact that inward advection of the flux mainly occurs at heights where the conductivity  $\eta^{-1}$  is high. This becomes important when an upper layer of the disk has a high conductivity (Bisnovaty-Kogan & Lovelace 2007; Rothstein & Lovelace 2008) or a high accretion velocity (Guilet & Ogilvie 2012, 2013).

## 2.2. Exterior-field Equation

Equation (6) requires a relation between  $\psi$  and the surface current density  $K_\phi$ . In this study, we follow LPP94a and determine  $K_\phi$  from Biot–Savart’s law. We assume that the current vanishes outside the disk (i.e., the exterior magnetic field is a potential field), and that the exterior field asymptotically approaches at infinity a uniform vertical field of strength  $B_\infty$ . Under these assumptions, the flux function  $\psi$  can be decomposed as (see Equation (17) of LPP94a)

$$\psi = \psi_\infty + \psi_d, \quad (10)$$

where

$$\psi_\infty(r) = \frac{1}{2} B_\infty r^2 \quad (11)$$

is the contribution from the imposed field and  $\psi_d$  is from the induced field. The latter is related to  $K_\phi$  via Biot–Savart’s law (LPP94a)<sup>2</sup>

$$\psi_d(r) = \frac{4}{c} \int R(r_<, r_>) K_\phi(r') dr', \quad (12)$$

$$R(r_<, r_>) \equiv r_> \left[ K\left(\frac{r_<}{r_>}\right) - E\left(\frac{r_<}{r_>}\right) \right], \quad (13)$$

where  $r_< = \min\{r, r'\}$ ,  $r_> = \max\{r, r'\}$ , and  $K(x)$  and  $E(x)$  are the complete elliptic integrals defined by  $K(x) = \int_0^{\pi/2} (1 - x^2 \sin^2 \theta)^{-1/2} d\theta$  and  $E(x) = \int_0^{\pi/2} (1 - x^2 \sin^2 \theta)^{1/2} d\theta$ . The set of Equations (6) and (12) determines the radial transport of the net poloidal flux in a disk under the assumptions we have employed.

## 2.3. Steady-state Condition

In this study, we focus on the steady-state solutions of Equations (6) and (12). For a steady state ( $\partial \psi / \partial t = 0$ ), Equation (6) gives the relation between  $B_z$  and  $K_\phi$ ,

$$B_z = \frac{2\pi D}{c} K_\phi, \quad (14)$$

<sup>2</sup> As shown in Appendix B, Equation (12) is equivalent to Equation (18) of LPP94a (see also Ogilvie 1997).

where the dimensionless coefficient  $D$  is defined as

$$D \equiv -\frac{\eta_*}{u_* H} = -\frac{2}{\int_{-H}^H (u_r/\eta) dz}. \quad (15)$$

Note that we have rewritten  $d\psi/dr$  in terms of  $B_z$  using Equation (2).

Equation (14) determines the bending angle of the poloidal field on the disk surface as a function of  $D$ . Substituting Equation (5) into Equation (7) and assuming that the poloidal field has dipolar symmetry, we have

$$K_\phi = \frac{c}{2\pi} B_{rs} - \frac{c}{4\pi} \frac{\partial}{\partial r} \int_{-H}^H B_z dz, \quad (16)$$

where  $B_{rs} \equiv B_r|_{z=H} (= -B_r|_{z=-H})$  is the radial field strength on the disk surface. If  $|B_{rs}/B_z| \gg H/r$ , the second term on the right-hand side of Equation (16) is negligible, so Equation (14) approximately gives

$$\frac{B_{rs}}{B_z} \approx \frac{1}{D}. \quad (17)$$

This equation implies that the poloidal field lines are bent by angle  $i$  from the vertical such that  $\tan i \approx 1/D$ . This well explains the numerical findings of LPP94a showing that  $\tan i = 1.52/(3D/2) = 1.01/D$  (see their Equation (40); note that  $D$  of LPP94a differs from our  $D$  by factor 2/3).

Equation (14) does not solely determine how each of  $B_{rs}$  and  $B_z$  depends on  $r$ . In order to know this, one needs to solve Biot-Savart's equation (Equation (12)) simultaneously with Equation (14). Section 3 will be devoted to this task.

#### 2.4. Assumption about $D$ and Definition of Regions

As mentioned earlier, recent theoretical studies have suggested that inward dragging of a poloidal field can efficiently take place in realistic accretion disks. We seek to understand how then a poloidal magnetic flux would be distributed in such a conductive disk. Unfortunately, the value of  $D$  is highly dependent on the vertical structure of an accretion disk, which is yet to be understood quantitatively. Therefore, in this study, we employ a simply toy model for the radial distribution of  $D$  as illustrated in Figure 2. Here, it is assumed that inward advection dominates over outward diffusion (i.e.,  $D < 1$ ) at  $r_{\text{in}} < r < r_{\text{out}}$ , and that the opposite happens (i.e.,  $D > 1$ ) at  $r < r_{\text{in}}$  and  $r > r_{\text{out}}$ . We will refer to the three regions as region I, II, and III from inside to outside (see Figure 2), and the quantities in different regions will be distinguished with subscripts ‘‘I,’’ ‘‘II,’’ and ‘‘III.’’ Region II corresponds to the body of a highly conducting disk, while region III may be regarded as the disk's outer edge where the ambipolar diffusivity is high ( $\eta_* \rightarrow \infty$ ) as suggested by Dzyurkevich et al. (2013). Region I may be considered as the central star where the accretion of matter terminates ( $u_* \rightarrow 0$ ). In reality, there can be a magnetosphere and a jet near the interface of the star and disk (Shu et al. 1994), but inclusion of these complexities is deferred to future work.

### 3. ANALYTIC STEADY SOLUTION

In this section, we derive the steady-state distribution of the poloidal field for the assumed distribution of  $D$ . We do this by solving Equations (14) and (12) analytically.

To make this problem analytically tractable, we for the moment approximate  $D$  as a piecewise smooth function with sharp transitions at  $r = r_{\text{in}}$  and  $r = r_{\text{out}}$  is sharp (see the dashed

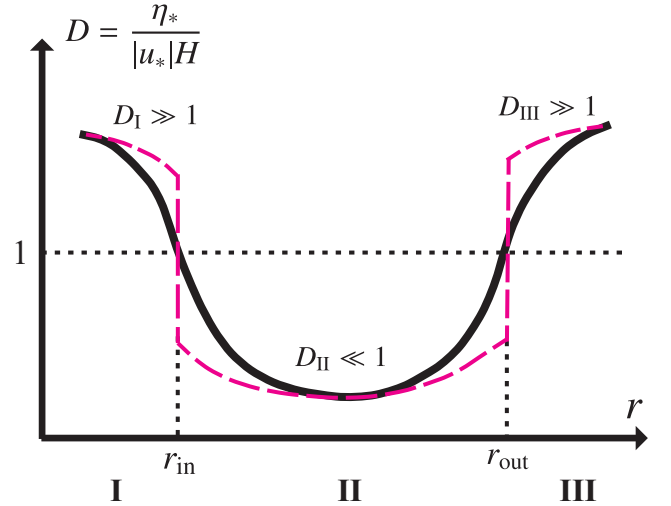


**Figure 2.** Schematic radial profile of  $D$  assumed in this study (solid curve). The disk is highly advecting ( $D \ll 1$ ) in the bulk of the disk (region II), with diffusion being dominant ( $D \gg 1$ ) only in the innermost and outermost parts of the disk (regions I and III). The three regions are defined by the boundaries where  $D$  crosses unity,  $r = r_{\text{in}}$  and  $r_{\text{out}}$ . The analytic steady solution derived in Section 3 approximates the boundaries as sharp transitions as depicted by the dashed curve. Smooth transitions like the solid curve will be considered in numerical calculations (Section 4.2).

line in Figure 2). Thus, in the following analysis,  $D$  is either  $\gg 1$  or  $\ll 1$ . The resulting analytic solution, however, approximates the solution for smooth  $D$  in a surprisingly good accuracy, as we will see in Section 4.2. In addition, we assume that the surface currents in regions I and III are so small that  $\psi_d$  is predominantly determined by the surface current in region II. Thus, we limit the interval of integration in Equation (12) to region II,  $r_{\text{in}} < r' < r_{\text{out}}$ . This is a good assumption since the surface current is generally suppressed in highly diffusive ( $D \gg 1$ ) regions.

The outline of our analysis is as follows. In Section 3.1, we expand variables and equations in powers of  $D_{\text{II}} (\ll 1)$ . This allows us to solve Equation (14) by successive substitution. We then identify in Section 3.2 how the leading-order quantities behave away from the boundaries ( $r_{\text{in}} \ll r \ll r_{\text{out}}$ ). We use the results to infer and derive the full solution for all regions, which will be done in Sections 3.3 and 3.4. Readers who are primarily interested in the final form of the solution and its implication can skip to Sections 3.4 and 3.5.

#### 3.1. Perturbative Expansion in Powers of $D_{\text{II}}$

Given  $D_{\text{II}} \ll 1$ , we are allowed to expand all the quantities and equations in powers of  $D_{\text{II}}$  and solve the equations perturbatively. Let us expand  $B_{z,\text{II}}$  and  $K_{\phi,\text{II}}$  as

$$B_{z,\text{II}} = B_{z,\text{II}}^{(0)} + B_{z,\text{II}}^{(1)} + O(D_{\text{II}}^2), \quad (18)$$

$$K_{\phi,\text{II}} = K_{\phi,\text{II}}^{(0)} + O(D_{\text{II}}), \quad (19)$$

where  $B_{z,\text{II}}^{(n)}, K_{\phi,\text{II}}^{(n)} = O(D_{\text{II}}^n)$  ( $n = 0, 1, \dots$ ), and similarly for all other variables in all regions.

Substituting Equations (18) and (19) into Equation (14) and collecting terms involving the same power of  $D_{\text{II}}$ , we obtain

$$B_{z,\text{II}}^{(0)} = 0, \quad (20)$$

$$B_{z,\text{II}}^{(1)} = \frac{2\pi D_{\text{II}}(r)}{c} K_{\phi,\text{II}}^{(0)} \quad (21)$$

to first order in  $D_{\text{II}}$ . Equation (20) means that region II is completely devoid of vertical fields in the limit of  $D_{\text{II}} \rightarrow 0$ . The vertical field strength is nonzero only to first order in  $D_{\text{II}}$ , and it is determined by the *zeroth-order* surface current  $K_{\phi, \text{II}}^{(0)}$ .

It follows from Equations (2) and (20) that  $\psi_{\text{II}}^{(0)}$  is independent of  $r$  and its value is determined by the flux inside region I, namely,

$$\psi_{\text{II}}^{(0)} = \psi(r_{\text{in}}) \equiv \psi_{\text{in}}, \quad (22)$$

where we have denoted the constant as  $\psi_{\text{in}}$ . From this and Equation (10), the disk-induced component of  $\psi_{\text{II}}^{(0)}$  is a quadratic function of  $r$ ,

$$\psi_{d, \text{II}}^{(0)}(r) = \psi_{\text{in}} - \psi_{\infty}(r) = \psi_{\text{in}} - \frac{1}{2}B_{\infty}r^2. \quad (23)$$

This means that to zeroth order in  $D_{\text{II}}$ , the disk-induced field ( $r^{-1}\partial\psi_{d, \text{II}}/\partial r$ ) in region II exactly cancels the imposed field ( $B_z$ ). Substituting (23) into the Biot–Savart equation (Equation (12)), we obtain the equation for  $K_{\phi, \text{II}}^{(0)}$ ,

$$\psi_{\text{in}} - \psi_{\infty}(r) = \frac{4}{c} \int_{r_{\text{in}}}^{r_{\text{out}}} R(r_{<}, r_{>}) K_{\phi, \text{II}}^{(0)}(r') dr', \quad (24)$$

where  $r_{\text{in}} < r < r_{\text{out}}$ . Note that we have neglected the current in regions I and III, as we already stated at the beginning of this section. The following subsections will be devoted to solving this equation.

### 3.2. Asymptotic Solution Deep Inside Region II

It is still not an easy task to find the solution to Equation (24). Therefore, it is useful to see how  $K_{\phi, \text{II}}^{(0)}$  behaves far away from the inner and outer boundaries. To do this, let us for the moment take the limits of  $r_{\text{in}} \rightarrow 0$  and  $r_{\text{out}} \rightarrow \infty$ . We also temporarily drop  $\psi_{\infty}(r)$  on the left-hand side of Equation (24) assuming that the induced component  $\psi_d$  dominates the total flux deep inside region II (this assumption will be validated a posteriori in Section 3.3). Under these simplifications, Equation (24) reduces to

$$\psi_{\text{in}} \approx \frac{4}{c} \int_0^{\infty} R(r_{<}, r_{>}) K_{\phi, \text{II}}^{(0)}(r') dr'. \quad (25)$$

The solution to Equation (25) can be easily found by assuming  $K_{\phi, \text{II}}^{(0)}$  of the power law from

$$K_{\phi}^{(0)}(r) = Ar^{-2}, \quad (26)$$

where  $A$  is a constant. For this  $K_{\phi, \text{II}}^{(0)}$ , the right-hand side of Equation (25) indeed becomes a constant,

$$\begin{aligned} & \frac{4A}{c} \int_0^{\infty} R(r_{<}, r_{>}) r'^{-2} dr' \\ &= \frac{4A}{c} \int_0^1 [K(x) - E(x)] (x^{-2} + x^{-1}) dx \\ &= \frac{2\pi A}{c}, \end{aligned} \quad (27)$$

where we have used that  $\int_0^1 [K(x) - E(x)] (x^{-2} + x^{-1}) dx = \pi/2$  (this can be proven with *Mathematica*). Comparing this with the left-hand side of Equation (25), we find

$$A = \frac{c\psi_{\text{in}}}{2\pi}. \quad (28)$$

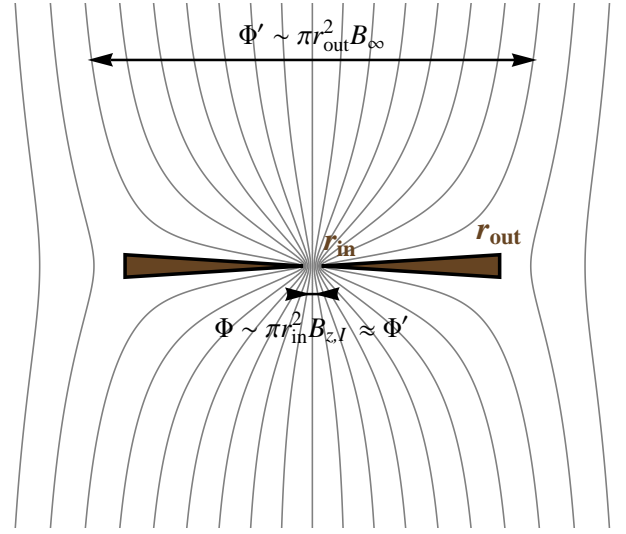


**Figure 3.** Split-monopole configuration of the magnetic field above and below a highly conductive ( $D \ll 1$ ) accretion disk. The gray wedges schematically show an edge-on view of the disk, and the thin solid curves are the exterior field lines. Away from the disk, the exterior field approaches the unidirectional imposed field  $B_{\infty}$ . At  $\sqrt{r^2 + z^2} \ll r_{\text{out}}$ , it approaches a monopolar field with the opposite polarity with respect to the equatorial plane. The magnetic flux threading at  $r \lesssim r_{\text{in}}$  is approximately equal to the flux of the imposed field threading at  $r \lesssim r_{\text{out}}$  (i.e.,  $\Phi \approx \Phi'$ ; see Equation (44)).

Consequently, we find that  $K_{\phi, \text{II}}^{(0)}$  at  $r_{\text{in}} \ll r \ll r_{\text{out}}$  asymptotically behaves as

$$K_{\phi, \text{II}}^{(0)}(r) \approx \frac{c\psi_{\text{in}}}{2\pi r^2}. \quad (29)$$

Equation (29) implies that the exterior field has a split-monopole geometry (see Figure 3). We recall that  $K_{\phi} \approx (c/2\pi)B_{rs}$  when  $B_{rs}/B_z \gg H/r$  (see Section 2.3). Thus, Equation (29) means that  $B_{rs} = \psi_{\text{in}}/r^2$  when  $D_{\text{II}} \ll 1$ . With this boundary condition and dipolar symmetry, potential theory tells us that the external field is a monopole field of strength  $|\mathbf{B}| = \psi_{\text{in}}/(r^2 + z^2)$  except that the field above the disk has the opposite sign to the field below. The split-monopole configuration is a natural consequence of flux accumulation at the center by a highly conductive ( $D \ll 1$ ) accretion disk (e.g., Galli & Shu 1993; Li & Shu 1997; Allen et al. 2003; Galli et al. 2006).

From Equation (29) and the steady-state condition (Equation (21)), the asymptotic form of  $B_{z, \text{II}}^{(1)}$  is

$$B_{z, \text{II}}^{(1)}(r) \approx \frac{D_{\text{II}}(r)\psi_{\text{in}}}{r^2}. \quad (30)$$

Note that  $B_{z, \text{II}}^{(1)}$  does not necessarily obey a power law since  $D_{\text{II}}$  is an arbitrary function of  $r$ .

It is also possible to find the asymptotic solution in region II for arbitrary values of  $D_{\text{II}}$  as long as it is a constant. We defer the demonstration of this to Appendix A because we will not use the results in the following analysis.

### 3.3. Determination of $\psi_{\text{in}}$

The asymptotic solution derived in Section 3.2 involves  $\psi_{\text{in}}$ , which is as yet undetermined. As we will show in this subsection, one can determine  $\psi_{\text{in}}$  by solving Equation (24) taking into account the presence of the imposed field,  $\psi_{\infty}$ .

Let us relax the condition  $r \ll r_{\text{out}}$  and instead assume  $K_{\phi, \text{II}}^{(0)}$

of the form

$$K_{\phi, \text{II}}^{(0)}(r) = \frac{c\psi_{\text{in}}}{2\pi r^2} f_{\text{out}}(r). \quad (31)$$

Here the correction factor  $f_{\text{out}}(r)$  satisfies  $f_{\text{out}} \rightarrow 1$  at  $r \ll r_{\text{out}}$  so that Equation (31) reduces to Equation (26) there. The equation to be solved is

$$\psi_{\text{in}} - \frac{1}{2}B_{\infty}r^2 = \frac{2\psi_{\text{in}}}{\pi} \int_0^{r_{\text{out}}} R(r_{<}, r_{>}) \frac{f_{\text{out}}(r')}{r'^2} dr'. \quad (32)$$

As we will show in Appendix B.2, the requirement that the right-hand side of Equation (32) be a quadratic function of  $r$  specifies  $f_{\text{out}}$  and  $\psi_{\text{in}}$ . We defer the derivation of it to the appendix and here only show the result. We find that  $f_{\text{out}}$  is well approximated by

$$f_{\text{out}}(r) = 1 + \frac{r}{r_{\text{out}}} \left\{ \left[ 1 - \left( \frac{r}{r_{\text{out}}} \right)^2 \right]^{\gamma} - 1 \right\}, \quad (33)$$

where  $\gamma = 0.45$  is the best-fit parameter. For this  $f_{\text{out}}$ , the right-hand side of Equation (32) becomes a quadratic form

$$\frac{2\psi_{\text{in}}}{\pi} \int_0^{r_{\text{out}}} R(r_{<}, r_{>}) K_{\phi, \text{II}}^{(0)}(r') dr' = \psi_{\text{in}} \left[ 1 - \frac{1}{2} \left( \frac{r}{r_{\text{out}}} \right)^2 \right]. \quad (34)$$

Finally, comparing this with the left-hand side of Equation (32), we find

$$\psi_{\text{in}} = B_{\infty} r_{\text{out}}^2. \quad (35)$$

It follows from Equation (35) that  $\psi_{\infty}(r) \ll \psi_{\text{in}}$  at  $r \ll r_{\text{out}}$ , which validates the assumption we made in Section 3.2.

Comparison between Equations (11) and (35) reveals an interesting relation

$$\psi_{\text{in}} = 2\psi_{\infty}(r_{\text{out}}). \quad (36)$$

In other words, the magnetic flux threading region I is exactly twice the flux of the *imposed* field threading regions I and II. One half of  $\psi_{\text{in}}$  simply means that the highly advecting region II flushes out all the imposed flux toward region I. Another half of  $\psi_{\text{in}}$  comes from region III: advection and diffusion near  $r = r_{\text{out}}$  do transport some fraction of the imposed flux in region III to region II. An important point here is that the latter process is however limited: even a highly conducting disk cannot convey an arbitrarily large poloidal flux from region III to region I. As we will see in Section 3.4, this fact sets an upper limit on the vertical field strength in region I.

For later convenience, we will also show how Equation (26) should be corrected near the inner boundary  $r = r_{\text{in}}$ . This correction becomes important when evaluating the magnetic flux inside region I (see Section 3.4). Let us assume  $K_{\phi, \text{II}}^{(0)} = (c\psi_{\text{in}}/2\pi r^2) f_{\text{in}}(r)$ , where  $f_{\text{in}}$  satisfies  $f_{\text{in}} \rightarrow 1$  at  $r \gg r_{\text{in}}$ . Substituting this into Equation (24) and assuming  $r_{\text{in}} \sim r \ll r_{\text{out}}$ , we obtain the equation for  $f_{\text{in}}$ ,

$$\psi_{\text{in}} = \frac{2\psi_{\text{in}}}{\pi} \int_{r_{\text{in}}}^{\infty} R(r_{<}, r_{>}) \frac{f_{\text{in}}(r')}{r'^2} dr'. \quad (37)$$

The left-hand side of this equation requires that the right-hand side be independent of  $r$ . As shown in Appendix B.2, this requirement specifies  $f_{\text{in}}$  as

$$f_{\text{in}}(r) = \left[ 1 - \left( \frac{r}{r_{\text{in}}} \right)^{-2} \right]^{-1/2}. \quad (38)$$

Note that  $f_{\text{in}}$  diverges at  $r = r_{\text{in}}$ , but the radially integrated current  $I_{\phi} = 2\pi \int r K_{\phi}(r) dr$  is still finite. The singularity merely reflects the sharp transition of the assumed  $D$  at  $r = r_{\text{in}}$ .

### 3.4. The Final Form of the Solution and an Example

To summarize the previous subsection, we have found that the surface current density in region II is given by

$$K_{\phi, \text{II}}(r) = \frac{cB_{\infty}}{2\pi} \left( \frac{r_{\text{out}}}{r} \right)^2 f_{\text{in}}(r) f_{\text{out}}(r). \quad (39)$$

This expression is correct to zeroth order in  $D_{\text{II}}$  (we will omit the superscripts “(0)” and “(1)” from this subsection onward). The correction factors  $f_{\text{in}}$  and  $f_{\text{out}}$  are given by Equations (38) and (33), respectively. These factors are only important near the inner and outer boundaries of region II, i.e.,  $f_{\text{in}} \approx 1$  at  $r \gg r_{\text{in}}$  and  $f_{\text{out}} \approx 1$  at  $r \ll r_{\text{out}}$ .

We are now able to derive the radial distribution of the induced field for all regions. For region II, Equations (39) and (21) give

$$B_{z, \text{II}} = D_{\text{II}} \left( \frac{r_{\text{out}}}{r} \right)^2 f_{\text{in}}(r) f_{\text{out}}(r) B_{\infty}, \quad (40)$$

to first order in  $D_{\text{II}}$ . For regions I and III, the Biot–Savart equation (Equation (12)) directly determines the induced flux as

$$\psi_{d, \text{I}}(r) = \frac{4}{c} \int_{r_{\text{in}}}^{r_{\text{out}}} R(r, r') K_{\phi, \text{II}} dr', \quad (41)$$

$$\psi_{d, \text{III}}(r) = \frac{4}{c} \int_{r_{\text{in}}}^{r_{\text{out}}} R(r', r) K_{\phi, \text{II}} dr', \quad (42)$$

where we have used that  $(r_{<}, r_{>}) = (r, r')$  for region I and  $(r_{<}, r_{>}) = (r', r)$  for region III. In Appendix C, we perform these integrations in an exact way and derive the analytic expressions for  $\psi_{d, \text{I}}$  and  $\psi_{d, \text{III}}$ . These are given by Equations (C6) and (C14), with the corresponding field strengths by Equations (C7) and (C15), respectively.

We are particularly interested in the vertical field strength in region I. Although its exact expression is given in Appendix C (Equation (C7)), it is more instructive to derive its asymptotic expression at  $r \ll r_{\text{in}}$  directly from Equation (41). For  $r \ll r_{\text{in}}$ , we may approximate the kernel  $R$  as  $R(r, r') \approx \pi r'^2/4r'$ , which follows from the asymptotic expansion of the elliptic integrals. We may also take  $r_{\text{out}} \rightarrow \infty$  and hence  $f_{\text{out}} \approx 1$  because the current at  $r \sim r_{\text{out}}$  has little effect on the magnetic flux at  $r \ll r_{\text{in}}$ . Using these approximations and Equations (39) and (41), we obtain

$$\begin{aligned} \psi_{d, \text{I}}(r) &\approx \frac{1}{2} B_{\infty} r_{\text{out}}^2 r^2 \int_{r_{\text{in}}}^{\infty} \frac{f_{\text{in}}(r')}{r'^3} dr' \\ &= \frac{1}{2} \left( \frac{r_{\text{out}}}{r_{\text{in}}} \right)^2 B_{\infty} r^2. \end{aligned} \quad (43)$$

Since  $\psi_{d, \text{I}} \gg \psi_{\infty}$ , we may approximate the total flux  $\psi$  with  $\psi_{d, \text{I}}$ . Substituting this into Equation (2), we finally obtain the vertical field strength deep inside region I,

$$B_{z, \text{I}} \approx \left( \frac{r_{\text{out}}}{r_{\text{in}}} \right)^2 B_{\infty}. \quad (44)$$

Note that  $B_{z, \text{I}}$  is independent of  $r$ , which is generally the case when diffusion dominates over advection.

Equation (44) is consistent with the idea that a high conducting disk transports all the imposed poloidal flux to region I (see Figure 3). We denote the flux of the magnetic field threading inside  $r < r_{\text{in}}$  by  $\Phi$  and the flux of the imposed field threading inside  $r < r_{\text{out}}$  by  $\Phi'$ . Since  $\Phi \sim \pi r_{\text{in}}^2 B_{z,\text{I}}$  and  $\Phi' \sim \pi r_{\text{out}}^2 B_{z,\infty}$ , Equation (44) implies that  $\Phi \approx \Phi'$ . This understanding is, however, only approximate as  $\Phi$  is in fact larger than  $\Phi'$  by a factor of 2 (see Equation (36)).

We also note that the correction factor  $f_{\text{in}}$  must be properly taken into account to derive the solution for  $B_{z,\text{I}}$  correctly. If one did not include the correction  $f_{\text{in}}$  in evaluating the integration in Equation (43), one would obtain  $\psi_{d,\text{I}} = (1/4)(r_{\text{out}}/r_{\text{in}})^2 B_{z,\infty} r^2$ , which is two times smaller than the correct expression in Equation (43).

So far we have neglected the current outside region II in evaluating the Biot–Savart equation. However, as  $B_{z,\text{I}}$  and  $B_{z,\text{III}}$  can be already known (from Equations (41) and (42)),  $K_{\phi,\text{I}}$  and  $K_{\phi,\text{III}}$  can be derived from the steady-state condition (Equation (14)), namely,

$$K_{\phi,\text{I}} = \frac{c}{2\pi D_{\text{I}}} B_{z,\text{I}}, \quad K_{\phi,\text{III}} = \frac{c}{2\pi D_{\text{III}}} B_{z,\text{III}}. \quad (45)$$

In fact, these are not necessarily small in magnitude when compared to  $K_{\phi,\text{II}}$ . However, this does not contradict our assumption because their contribution to the induced flux is indeed negligible as long as  $D_{\text{II}} \ll 1$ .

As an example, we illustrate in Figure 4 the steady solution for the case of  $r_{\text{in}} = 0.01 r_{\text{out}}$ ,  $D_{\text{I}} = D_{\text{III}} = 30$ , and  $D_{\text{II}} = 0.03$ . The same set of parameters will be considered in Section 4 where we will compare the analytic steady solution with time-dependent solutions from direct numerical integration. We will see that this steady solution is indeed materialized as a result of time evolution.

### 3.5. Maximum Field Strength as a Function of $r$

An important implication of the steady-state solution is the presence of an *upper limit* on the vertical field strength  $B_z$  attainable in steady states. To see this, let us consider how  $B_z$  at a fixed position  $r$  ( $< r_{\text{out}}$ ) changes with changing the position of the inner boundary  $r_{\text{in}}$ . We neglect the correction factors  $f_{\text{in}}$  and  $f_{\text{out}}$  as they become important only when  $r$  is very close to  $r_{\text{in}}$  or  $r_{\text{out}}$  (furthermore, we will see in Section 4.2 that the features of these correction factors are smeared when  $D$  is smooth). Then, from Equations (40) and (44), we find

$$B_z = \begin{cases} \left(\frac{r_{\text{out}}}{r_{\text{in}}}\right)^2 B_{z,\infty}, & r < r_{\text{in}} \text{ (region I)}, \\ D(r) \left(\frac{r_{\text{out}}}{r}\right)^2 B_{z,\infty}, & r > r_{\text{in}} \text{ (region II)}. \end{cases} \quad (46)$$

Now let us view this as a function of  $r_{\text{in}}$  and observe how  $B_z$  varies as  $r_{\text{in}}$  varies from  $> r$  to  $< r$ . For  $r_{\text{in}} > r$ ,  $B_z$  monotonically increases with decreasing  $r_{\text{in}}$  and reaches a maximum  $(r_{\text{out}}/r)^2 B_{z,\infty}$  at  $r_{\text{in}} = r$ . Once  $r_{\text{in}}$  falls below  $r$ ,  $B_z$  does not exceed this value any more since  $D < 1$  in region II. Thus, in the steady states,  $B_z$  at a given position is bounded from above by

$$B_{z,\text{max}}(r) = \left(\frac{r_{\text{out}}}{r}\right)^2 B_{z,\infty}. \quad (47)$$

Note that Equation (47) does not apply to region III ( $r > r_{\text{out}}$ ), where  $B_z \approx B_{z,\infty}$  (see Figure 4(c)). The dashed line in Figure 4(c) indicates Equation (47) for  $r < r_{\text{out}}$ .

## 4. COMPARISON WITH NUMERICAL SOLUTIONS

In this section, we test the steady-state solution obtained in Section 3 with numerical calculations of the original evolution equation (Equation (6)). We integrate Equations (6) and (12) using the finite-volume method described by LPP94a. We set  $r_{\text{in}} = 0.01 r_{\text{out}}$  and take the computational domain to be  $r_{\text{min}} \leq r \leq r_{\text{max}}$  with  $r_{\text{min}} = 0.03 r_{\text{in}}$  and  $r_{\text{max}} = 30 r_{\text{out}}$ . The domain is divided into 400 logarithmically spaced cells. We use a zero-flux boundary condition for the inner boundary (i.e.,  $\partial\psi/\partial t = 0$  at  $r = r_{\text{min}}$ ), while for the outer boundary we allow the magnetic flux to flow across it by assuming that  $B_z = B_{z,\infty}$  (or equivalently  $\partial\psi/\partial r = r B_{z,\infty}$ ) at  $r = r_{\text{max}}$ .

The time-dependent problem requires either  $\eta_*$  or  $u_*$  to be given in addition to  $D$ . Here we prescribe  $\eta_*$  to be a quadratic function of  $r$ ,  $\eta_*(r) = r^2/t_*$ , where the constant  $t_*$  has the dimension of time. The radial distribution of  $u_*$  is then determined according to the definition of  $D$  (Equation (15)), i.e.,  $u_* = -\eta_*/(DH)$ . Thus, the advection speed  $|u_*|$  is small in regions I and III and is large in region II. The disk thickness  $H$  is taken so that the disk aspect ratio  $h \equiv H/r$  is 0.1 for all  $r$ . All these input parameters are assumed to be independent of time  $t$  for simplicity. This restriction will be relaxed in Paper II.

The initial condition is specified by the initial distribution of the disk-induced flux  $\psi_d$ . Fiducially we will take  $\psi_d(t = 0) = 0$  (i.e.,  $B_z = B_{z,\infty}$ ) throughout the computational domain, but will also consider the case where the innermost region (region I) initially possesses an induced field in excess of the steady-state value.

In the following subsections, we consider two model functions for  $D$  and present the results for each model.

### 4.1. Piecewise Constant $D$

The first model for  $D$  is a piecewise constant function given by  $D_{\text{I}} = D_{\text{III}} = 30$  and  $D_{\text{II}} = 0.03$ . This has already been used in Section 3.4 for an illustrative purpose. The radial profile of  $D$  is shown in Figure 4(a). For the initial condition, we adopt either  $B_z = B_{z,\infty}$  for all  $r$  (case A) or  $B_z = 10^6 B_{z,\infty}$  for  $r < r_{\text{in}}$  and  $B_z = B_{z,\infty}$  for  $r > r_{\text{in}}$  (case B).

Figures 5(a) and (b) display the results for the two different initial conditions (cases A and B, respectively). The dotted curves are the initial profiles of  $B_z$ , and the thin solid curves are the analytic steady solution for the assumed  $D$  (also shown in Figure 4(b)). For both cases, we find that the time-dependent numerical solution approaches the analytic steady solution after a sufficient time. The only important difference is that region I gains the flux in case A while it loses the initial excess flux in case B. Thus, any vertical flux in excess of the steady-state value diffuses away with time. It should be noted that details of the time evolution depend on the assumption about  $\eta_*$  and are therefore not important here.

### 4.2. Smooth $D$

So far we have assumed that  $D$  sharply varies at the boundaries of region II. We here examine whether our steady solution is applicable even when  $D$  smoothly connects between advective ( $D < 1$ ) and diffusive ( $D > 1$ ) regions. We adopt a continuous function  $\log D = 1.5 \tanh[3 \log(r/r_{\text{in}})] \tanh[3 \log(r/r_{\text{out}})]$ . This smoothly crosses unity at  $r = r_{\text{in}}$  and  $r = r_{\text{out}}$  as depicted in the top panel of Figure 6. For this model, we predict the steady-state profile of  $B_z$  in the same way as we did for piecewise constant  $D$ , i.e., by applying Equations (C7), (40), and (C15) for regions I, II, and III, respectively. The predicted

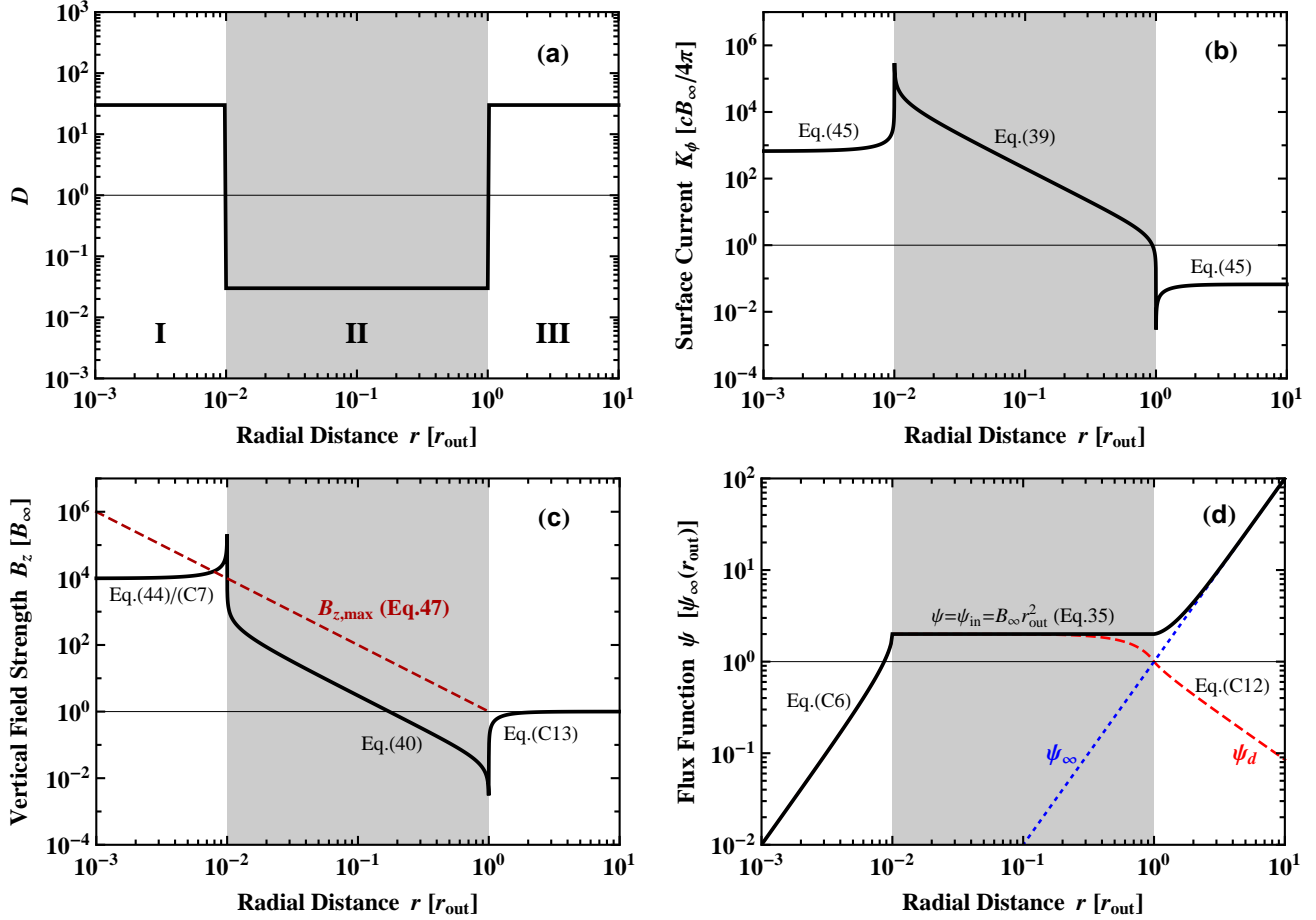


**Figure 4.** Steady-state solution for a piecewise constant  $D$ . The inner boundary of region II is set to  $r_{\text{in}} = 0.01r_{\text{out}}$ . Panel (a) displays the assumed radial profile ( $D_{\text{I}} = D_{\text{III}} = 0.03$ , and  $D_{\text{II}} = 30$ ). Panels (b), (c), and (d) show the surface current density  $K_\phi$ , vertical field strength  $B_z$ , and flux function  $\psi$ , respectively. The flux function is the sum of the contributions from the imposed fields,  $\psi_\infty$  (dotted curve), and from the induced field,  $\psi_d$  (dashed curve). Note that the spikes and valleys in the plots of  $B_z$  and  $K_\phi$  merely reflect the discontinuities of the assumed  $D$  at the boundaries  $r = r_{\text{in}}$  and  $r_{\text{out}}$ ; these features do not appear when  $D$  is smooth (see Section 4.2 and Figure 6).

profile of  $B_z$  is shown in the middle panel of Figure 6 with a solid curve. Note that the profile of  $B_z$  deep inside region II ( $r_{\text{in}} \ll r \ll r_{\text{out}}$ ) is no longer given by a power law because of the radial dependence of  $D$ .

We compare this with the numerical solution of the time-dependent problem with the initial condition  $B_z = B_\infty$ . We again see that the analytic solution well reproduces the numerical solution at late times. One exception is that the numerical solution has no visible spike or valley in  $B_z$  near  $r = r_{\text{in}}$  and  $r = r_{\text{out}}$  (see Figure 5). One might expect that the value of  $\psi$  in region II should be smaller than the prediction from the analytic solution because the peak of  $B_z$  is absent at  $r = r_{\text{out}}$ . However, inspection of  $\psi$  shows that its steady-state value agrees with the prediction  $2\psi_\infty(r_{\text{out}})$  (Equation (35)) as long as one measures it slightly outside  $r = r_{\text{out}}$ . This suggests that the sharp peak in  $B_z$  is not removed but rather smeared out by the smoothed  $D$  profile. Therefore, we conclude that our analytic steady-state solution is applicable even when  $D$  is a smooth function of  $r$ , except for smeared structures near the positions where  $D = 1$ .

## 5. APPLICATION TO PROTOPLANETARY DISKS

In Section 3.5, we have derived the maximum strength on the vertical field strength in steady states. We here apply this result to protoplanetary disk systems and discuss its

astrophysical implications. As a reference value, we take  $r_{\text{out}} = 100$  AU from millimeter observations of T Tauri disks (e.g., Kitamura et al. 2002; Andrews et al. 2009), and  $B_\infty = 10 \mu\text{G}$  from Zeeman observations of molecular clouds (e.g., Troland & Crutcher 2008; Crutcher et al. 2009). Then, Equation (47) predicts

$$B_{z,\text{max}}(r) = 0.1 r_{\text{AU}}^{-2} \left( \frac{r_{\text{out}}}{100 \text{ AU}} \right)^2 \left( \frac{B_\infty}{10 \mu\text{G}} \right) \text{G}, \quad (48)$$

where  $r_{\text{AU}} = r/(1 \text{ AU})$ . The solid line in Figure 7 shows the radial distribution of  $B_{z,\text{max}}$  for the case of  $B_\infty = 10 \mu\text{G}$  and  $r_{\text{out}} = 100$  AU.

In protoplanetary disks, the magnetic pressure given by Equation (48) is much smaller than the gas pressure unless the disk gas is significantly depleted. In this sense, the large-scale field itself has no effect on the dynamics of the gas disks near the midplane. For example, if we take the gas pressure distribution from the minimum-mass solar nebula model of Hayashi (1981) and the magnetic pressure from Equation (48), then the gas-to-magnetic pressure ratio (or the plasma beta) at the midplane is  $\sim 10^6$  at  $r = 100$  AU and  $\sim 10^4$  at  $r = 0.1$  AU. However, MRI and disk winds induced by the large-scale field do have a significant effect on disk evolution. We will see this in Section 5.1.



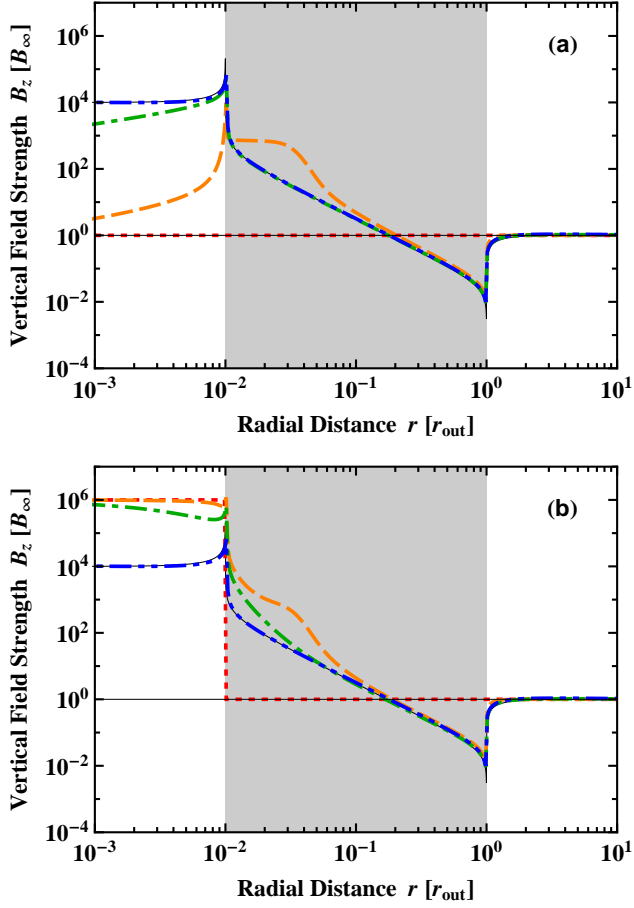


**Figure 5.** Comparison between analytic and time-dependent numerical solutions of Equations (6) and (12) for piecewise constant  $D$  (Section 4.1; see Figure 4(a) for the radial profile of the assumed  $D$ ). Panel (a) shows the result for the initial condition  $B_z = B_\infty$ , while in the simulation shown in panel (b) the initial  $B_z$  is augmented by factor  $10^6$  at  $r < r_{\text{in}}$ . The dotted lines show the initial condition. The dashed, dot-dashed, and dot-dot-dashed lines are the snapshots of the numerical solutions at times  $t = 0.01t_*$ ,  $0.1t_*$ , and  $1.0t_*$ , respectively. The solid lines are the analytic steady-state solution derived in Section 3 (also shown in Figure 4(b)). Note that the snapshots for  $t = 1.0t_*$  and analytic solution are almost indistinguishable.

### 5.1. Upper Limits on the Accretion Rate

The primary purpose of this study is to understand the evolution of protoplanetary disks in the framework of magnetic accretion scenarios. As mentioned earlier, both MRI-driven and wind-driven accretion mechanisms predict that the mass accretion rate  $\dot{M}$  depends on the strength of the net (large-scale) vertical field. In this subsection, we synthesize Equation (48) and existing theoretical predictions for the  $\dot{M}$ – $B_z$  relation to constrain the range of the accretion rate attainable by these accretion mechanisms.

Because protoplanetary disks are poorly ionized, MRI and winds in the disks are highly susceptible to non-ideal MHD effects. Lacking an established accretion model accounting for all the non-ideal effects, we employ two existing models in parallel. We first consider the classical scenario where only ohmic diffusion is taken into account. For this case, Okuzumi & Hirose (2011) empirically obtained the  $\dot{M}$ – $B_z$  relation for MRI-driven turbulence. They found that if ohmic diffusion suppresses MRI near the midplane then the relation

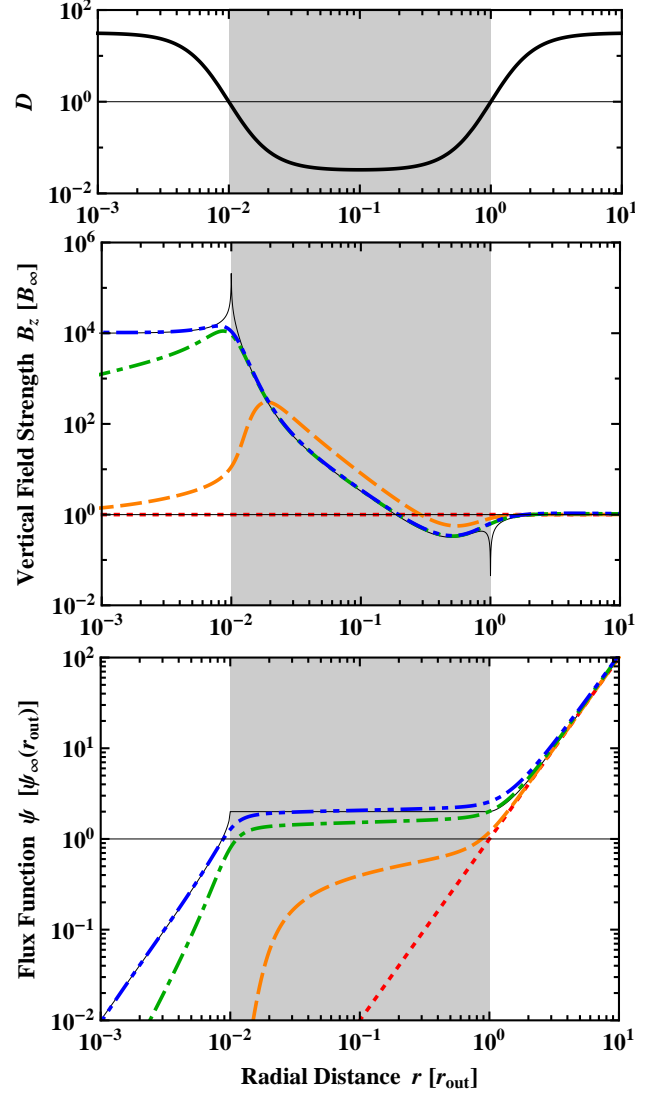


**Figure 6.** Comparison between analytic and time-dependent numerical solutions of Equations (6) and (12) for smooth  $D$  (Section 4.2). The top panel shows the assumed  $D$ , and the middle and bottom panels show the result. The initial condition is  $B_z = B_\infty$  for all  $r$  (dotted line). The dashed, dot-dashed, and dot-dot-dashed lines are the snapshots of the numerical calculations at  $t = 0.01t_*$ ,  $0.1t_*$ , and  $1.0t_*$ , respectively.

is given by<sup>3</sup>

$$\alpha \approx 530\beta_{z0}^{-1}. \quad (49)$$

Here  $\alpha$  is the height-averaged turbulent stress normalized by the height-averaged pressure (also known as the Shakura–Sunyaev  $\alpha$  parameter), and  $\beta_{z0}$  is the plasma beta for the net vertical flux measured at the midplane. In steady states,  $\alpha$  is related to  $\dot{M}$  as  $\dot{M} = 2\pi\alpha\Sigma c_s^2/\Omega$ , where  $\Omega$  is the orbital frequency,  $\Sigma$  is the gas surface density, and  $c_s$  is the sound speed (see, e.g., Section III.A of Balbus & Hawley 1998; Equation (19) of Simon et al. 2013a). The midplane plasma beta is related to the net vertical field strength  $B_z$  as  $\beta_{z0} = 8\pi\Sigma c_s^2/\sqrt{2\pi}B_z^2 H_g$ , where  $H_g = c_s/\Omega$  is the pressure scale height of the disk. If we use these relations, Equ-

<sup>3</sup> Equation (49) follows from the relations  $\alpha = \alpha_{\text{core}} + \alpha_{\text{atm}}$ ,  $\alpha_{\text{atm}} \gg \alpha_{\text{core}}$ , and  $\alpha_{\text{atm}} \approx 530\beta_{z0}^{-1}$ , which hold when the MRI-dead zone is thick (for details, see Section 5.2 of Okuzumi & Hirose 2011).

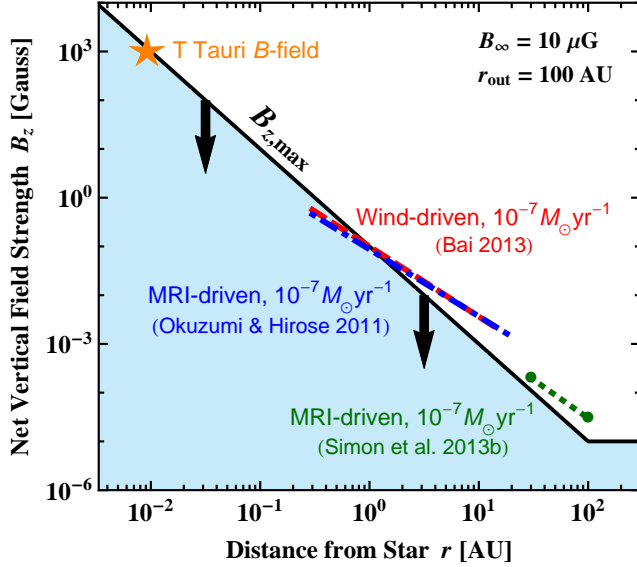


**Figure 7.** Upper limit on the large-scale vertical field strength,  $B_{z,\max}$  (Equation (48); solid line), for  $B_\infty = 10 \mu\text{G}$  and  $r_{\text{out}} = 100 \text{ AU}$ . The dot-dashed, dashed, and dotted lines show theoretical predictions for the vertical field strength required for disk accretion of  $\dot{M} = 10^{-7} M_\odot \text{ yr}^{-1}$  (see Section 5.1 for details). The star symbol marks the typical field strength and radius of observed T Tauri stars.

tion (49) translates into the  $\dot{M}$ – $B_z$  in physical units,

$$\dot{M} \approx 330 \frac{H_g}{\Omega} B_z^2. \quad (50)$$

Note that  $\dot{M}$  is independent of the disk mass since  $\alpha \propto \dot{M}/\Sigma$  while  $\beta_{z0} \propto \Sigma/B_z^2$ . This reflects the fact that the Maxwell stress does not explicitly involve the gas density (see Wardle 2007 and Bai 2011 for a similar expression).

Let us see how  $B_{z,\max}$  constrains the accretion rate given by Equation (50). Here we assume a protoplanetary disk around a solar-type star and adopt  $\Omega = 2.0 \times 10^{-7} r_{\text{AU}}^{-3/2} \text{ s}^{-1}$  and  $H_g = 0.033 r_{\text{AU}}^{5/4} \text{ AU}$  following Hayashi (1981). Substituting these into Equation (50), we obtain

$$\dot{M} \approx 1.3 \times 10^{-7} r_{\text{AU}}^{11/4} \left( \frac{B_z}{0.1 \text{ G}} \right)^2 M_\odot \text{ yr}^{-1}. \quad (51)$$

This gives the MRI-driven accretion rate for given  $B_z$ . Applying the constraint  $B < B_{z,\max}$  to the above relation, we obtain  $\dot{M} \lesssim 1 \times 10^{-7} M_\odot \text{ yr}^{-1}$  at  $r = 1 \text{ AU}$  and  $\dot{M} \lesssim 0.7 \times 10^{-8} M_\odot \text{ yr}^{-1}$  at  $r = 10 \text{ AU}$ . The dot-dashed line in Figure 7 shows the value of  $B_z$  required for  $\dot{M} = 10^{-7} M_\odot \text{ yr}^{-1}$  predicted by Equation (51).

A similar constraint is derived from the more recent scenario including ambipolar diffusion. Recent MHD simulations by Bai & Stone (2013b) and Bai (2013) have suggested that accretion at  $0.3 \text{ AU} \lesssim r \lesssim 15 \text{ AU}$  is mainly driven by magnetocentrifugal winds because ambipolar diffusion completely suppressed MRI there. The relation between the wind-driven  $\dot{M}$  and  $B_z$  has been provided by Bai (2013), which reads<sup>4</sup>

$$\dot{M} = 0.47 \times 10^{-8} r_{\text{AU}}^{1.90} \left( \frac{B_z}{10 \text{ mG}} \right)^{1.32} M_\odot \text{ yr}^{-1}. \quad (52)$$

<sup>4</sup> Bai (2014) reports that Equation (11) of Bai (2013) was provided with error. Here we use the correct result given by Bai (2014, his Equation (33)).

Note that  $\dot{M}$  is again independent of  $\Sigma$  (see Bai 2013 for more discussions). If we apply  $B < B_{z,\max}$  to Equation (52), we obtain  $\dot{M} \lesssim 1 \times 10^{-7} M_\odot \text{ yr}^{-1}$  at  $r = 1 \text{ AU}$  and  $\dot{M} \lesssim 2 \times 10^{-8} M_\odot \text{ yr}^{-1}$  at  $r = 10 \text{ AU}$ . The dashed line shows the value of  $B_z$  required for  $\dot{M} = 10^{-7} M_\odot \text{ yr}^{-1}$  predicted by Equation (52).

Farther out in the disks, MRI operates even in the presence of ambipolar diffusion. MHD simulations by Simon et al. (2013b) show that  $\dot{M}$  increases with  $B_z$  and reaches  $10^{-7} M_\odot \text{ yr}^{-1}$  at  $B_z \sim 200 \mu\text{G}$  for  $r = 30 \text{ AU}$ , and at  $30 \mu\text{G}$  for  $r = 100 \text{ AU}$ . These values are marked in Figure 7 by the filled circles connected by the dotted line. We find that the required field strengths are close to the upper limit  $B_{z,\max}$ , which suggests that  $\dot{M} \lesssim 10^{-7} M_\odot \text{ yr}^{-1}$  for these regions.

Taken together, all these models suggest that the upper limit on the magnetically driven accretion rate is  $\sim 10^{-7} M_\odot \text{ yr}^{-1}$ . This is consistent with upper limits suggested by observations (Hartmann et al. 1998; Calvet et al. 2004; Sicilia-Aguilar et al. 2005).

## 5.2. Possible Relevance to the “Magnetic Flux Problem” in Star Formation

Another interesting application of Equation (48) is to the so-called magnetic flux problem in star formation (Nakano 1984). Young stars are known to have a magnetic field of typical strength  $\sim \text{kG}$  (e.g., Johns-Krull 2007). Star-forming dense cores of molecular clouds also have a magnetic field (Troland & Crutcher 2008; Crutcher et al. 2009), but the magnetic flux of a single core is about four orders of magnitude larger than that of a single young star. Therefore, the magnetic flux that was inherited from the parent cloud must have dissipated, at least to a  $\lesssim \text{kG}$  level, by the time the star became visible. ohmic dissipation during star formation is one plausible solution to this problem (e.g., Nakano et al. 2002; Shu et al. 2006; Machida et al. 2007; Dapp et al. 2012). Other possibilities include flux destruction after the external field detaches from the star (Braithwaite 2012).

Here we explore the possibility that the excess flux is lost through transport between the star and surrounding protoplanetary disk. Let us suppose that a protoplanetary disk extends to a central star and hence Equation (48) is applicable down to the interface between the disk and star. Then, Equation (48) suggests that  $B_{z,\max} \approx 1 \text{ kG}$  at protostellar radius  $\approx 2R_\odot \approx 10^{-2} \text{ AU}$  for the selected parameters  $B_\infty = 10 \mu\text{G}$  and  $r_{\text{out}} = 100 \text{ AU}$  (see the star symbol in Figure 7). Interestingly, the predicted  $B_{z,\max}$  is in good agreement with the observed stellar field strengths. Any excess flux above this level will be lost after a sufficient time (as demonstrated in Figure 5(b)) if the flux transport is allowed across the star–disk interface (for example, convection inside the star might effectively diffuse the flux toward the stellar surface). If this mechanism is viable, then this might partly resolve the long-standing problem of star formation theory. Further examination of this possibility will require a more detailed model for the star–disk interface (e.g., a magnetosphere and a jet will need to be taken into account), which is beyond the scope of this paper.

## 6. SUMMARY AND DISCUSSION

We have studied how a large-scale poloidal field is transported in a highly conducting accretion disk, primarily aiming at understanding the viability of magnetically driven accretion mechanisms. We have employed the kinematic mean-field

model for a large-scale poloidal field originally developed by LPP94a. As a first step, we have focused on steady states where inward advection of a poloidal field balances with outward diffusion. In a companion paper (Takeuchi & Okuzumi 2014), we extend our analysis to time-dependent problems and study how poloidal fields are transported in evolving accretion disks.

We have analytically derived the steady-state distribution of a poloidal field for conducting accretion disks. The most important finding from this solution is that there is an upper limit on the large-scale vertical field strength attainable in steady states (Equation (47)). The upper limit is given by a function of the distance from the central star ( $r$ ), the poloidal strength at infinity ( $B_\infty$ ), and the outer radius of the highly conductive region ( $r_{\text{out}}$ ). For  $r_{\text{out}} = 100$  AU and  $B_\infty = 10 \mu\text{G}$ , the maximum vertical field strength is about 0.1 G at  $r = 1$  AU, and about 1 mG at  $r = 10$  AU (Equation (48); Figure 7). Any poloidal field of a strength above the limit will eventually diffuse away outward on the diffusion timescale. We have demonstrated this with time-dependent numerical calculations of the mean-field equations.

We have applied this upper limit to a large-scale poloidal field threading a protoplanetary disk around a young star. We have adopted three different theoretical models for magnetically driven accretion (Okuzumi & Hirose 2011; Bai 2013; Simon et al. 2013b) to translate the large-scale vertical field strength into the accretion rate. All three models suggest a maximum steady-state accretion rate of  $\sim 10^{-7} M_\odot \text{yr}^{-1}$ . This is in agreement with observations showing that  $\dot{M} \sim 10^{-9} - 10^{-7} M_\odot \text{yr}^{-1}$  for T Tauri stars.

We have also applied the upper limit to the flux of young stars assuming that surrounding disks extend to the stellar surface. We find that the maximum field strength is  $\sim 1$  kG at the surface of the central star. This implies that any excess stellar poloidal field of strength  $\gtrsim$  kG can be lost via outward diffusion to the circumstellar disks. That mechanism might explain why observed young stars have a significantly small magnetic flux compared to molecular cloud cores. Further examination of this possibility will await a detailed model for the gas dynamics on the star-disk boundary.

As already pointed out by Ogilvie & Livio (2001), the details of the steady-state solution depend on the vertical structure of the disk through the dimensionless quantity  $D$  (Equation (15)). Although recent studies suggest  $D < 1$  (see the introduction), the precise value of  $D$  is still uncertain for real accretion disks. This is particularly true for protoplanetary disks, where non-ideal MHD effects are likely to affect the value of it. In this study, we have assumed  $D \ll 1$  for the bulk of the disks motivated by the fact that otherwise the vertical magnetic flux would become too small to affect disk evolution (Bai & Stone 2013b; Simon et al. 2013a). This assumption needs to be justified with MHD simulations that take into account the ionization structure of the disks in the vertical direction. Very recently, Bai & Stone (2013b) and Bai (2013) have conducted such simulations, and the results show that the poloidal field is significantly bent on the disk surface, i.e.,  $B_{r\theta} > B_z$  (see Figures 10 and 11 of Bai & Stone 2013b). This, together with Equation (17) in this paper, suggests that  $D < 1$  is possible in protoplanetary disks even in the presence of non-ideal MHD effects.

The present study has employed a number of simplifications, and there are at least three important caveats that should be mentioned. First, all important parameters have been treated as time independent, but this assumption breaks down

when the gas disk evolves faster than the poloidal field. If this is the case, the poloidal-field distribution largely depends on the initial condition, as we will discuss in a companion paper (Takeuchi & Okuzumi 2014). Second, we have assumed that the toroidal current vanishes in the exterior of the disk and approximated the exterior field as a potential field. However, it is not obvious how this approximation applies when a magnetocentrifugal wind is present. This issue was already noted and discussed in detail by Ogilvie (1997). He showed that the Biot-Savart equation precisely describes the exterior field as long as the field inside the Alfvén surface of the wind is considered. However, the asymptotic field  $B_\infty$  must then be regarded as including the contribution from the toroidal currents beyond the Alfvén surface. This contribution was neglected in this study and therefore will need to be quantified in future work. Finally, it is not always true that a steady state is reached as a result of disk-field evolution. For example, some models predict that wind-driven accretion is unstable (Lubow et al. 1994b; Cao & Spruit 2002; Moll 2012).

We thank Takeru Suzuki, Shu-ichiro Inutsuka, and Hidekazu Tanaka for inspiring discussion. We also thank the anonymous referee for comments that clarified the paper. This work was supported by Grant-in-Aid for Research Activity Start-up (#25887023, 24840037) from JSPS, and by Grants-in-Aid for Scientific Research (#20540232, 23103005) from MEXT.

*Note added in proof.* Recently, Guilet & Ogilvie (2014) have independently studied the radial transport of large-scale poloidal fields in protoplanetary disks. Their mean-field approach is essentially the same as ours, although they also consider cases where the transport coefficients ( $u_*$  and  $\eta_*$ ) depend on the vertical field strength. For the cases where the transport coefficients are independent of the field strength, their results are consistent with ours; in particular, we have numerically verified that their self-similar steady solution (their Equation (31)) is precisely equivalent to ours (our Equation (A7)).

## APPENDIX

### A. ASYMPTOTIC SOLUTION IN REGION II FOR ARBITRARY CONSTANT $D_{\text{II}}$

In this appendix, we consider cases where  $D_{\text{II}}$  is constant but not necessarily small. For these cases, Equations (12) and (14) become self-similar with respect to  $r$  in the limit of  $r_{\text{in}} \ll r \ll r_{\text{out}}$  and  $\psi_\infty \ll \psi_d$ , and therefore the solution must be written as a power law. Specifically, if we suppose  $K_\phi \propto r^{-q}$  with  $q$  being a constant, then a dimensional analysis shows  $B_z \propto r^{-q}$  and  $\psi \propto r^{2-q}$ . As we will see below, the exponent  $q$  is determined as a function of  $D_{\text{II}}$ .

Below we omit the subscript ‘‘II’’ for the sake of clarity. In the limit of  $r_{\text{in}} \ll r \ll r_{\text{out}}$  and  $\psi_\infty \ll \psi_d$ , Equation (12) reduces to

$$\psi = \frac{4}{c} \int_0^\infty R(r_<, r_>) K_\phi(r') dr'. \quad (\text{A1})$$

Note that the perturbative approach employed in Section 3.1 is not used here as it only applies to  $D \ll 1$ . Let us assume

$$K_\phi(r) = Ar^{-q}, \quad (\text{A2})$$

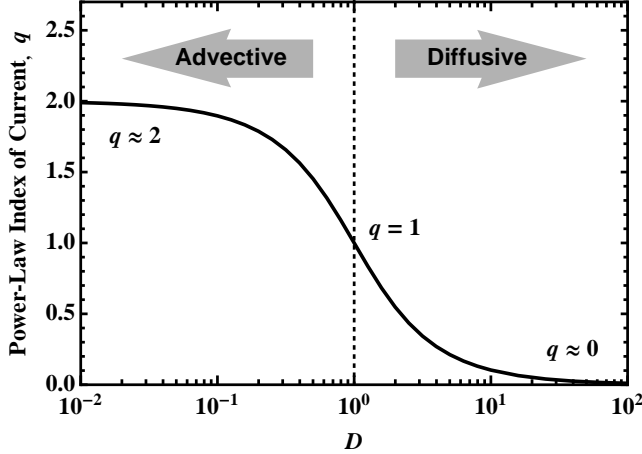


Figure 8. Power-law index  $q$  for radially constant  $D$ .

where  $A$  and  $q$  are constants. Substituting Equation (A2) into Equation (A1), we obtain

$$\psi = \frac{2\pi C(q)}{c} A r^{2-q}, \quad (\text{A3})$$

where

$$C(q) \equiv \frac{2}{\pi} \int_0^1 [K(x) - E(x)] (x^{-q} + x^{q-3}) dx \quad (\text{A4})$$

is a numerical coefficient that depends on  $q$ . For  $0 < q < 3$ , the integration on the right-hand side of Equation (A4) converges, resulting in

$$C(q) = \frac{2}{3\pi} \left[ {}_3F_2 \left( 1, 1, \frac{4-q}{2}; \frac{3}{2}, \frac{5}{2}; 1 \right) + {}_3F_2 \left( 1, 1, \frac{q+1}{2}; \frac{3}{2}, \frac{5}{2}; 1 \right) \right], \quad (\text{A5})$$

where  ${}_3F_2$  is a generalized hypergeometric function. It is useful to note that  $C(1) = C(2) = 1$ .

The induced vertical field is

$$\begin{aligned} B_z &= \frac{1}{r} \frac{d\psi}{dr} = \frac{2\pi(2-q)C(q)}{c} A r^{-q} \\ &= \frac{2\pi(2-q)C(q)}{c} K_\phi. \end{aligned} \quad (\text{A6})$$

Comparing this with Equation (14), we obtain the equation for  $q$ ,

$$(2-q)C(q) = D. \quad (\text{A7})$$

Figure 8 plots the solution of Equation (A7) as a function of  $D$ . We see that  $q$  monotonically increases with decreasing  $D$ , meaning that the radial profiles of  $B_z$  and  $K_\phi$  become steeper as inward advection becomes more effective. The asymptotic values are  $q \rightarrow 2$  for  $D \rightarrow 0$  and  $q \rightarrow 0$  for  $D \rightarrow \infty$ . The solution for  $D \rightarrow \infty$  just shows that the vertical field strength becomes uniform in  $r$  in the limit where diffusion dominates over advection.

## B. INVERTING BIOT-SAVART'S INTEGRAL EQUATION

In this appendix, we present an analytic method to invert Biot–Savart's equation. In an integral form, the Biot–Savart's

law can be written as (see, e.g., Jackson 1998)

$$\frac{\psi_d(r)}{r} = \frac{1}{c} \int_{r_{\text{in}}}^{r_{\text{out}}} r' dr' \int_0^{2\pi} d\phi' \frac{K_\phi(r') \cos \phi'}{(r^2 + r'^2 - 2rr' \cos \phi')^{1/2}} \quad (\text{B1})$$

(as shown below, this is equivalent to Equation (12) in the main text). We seek a  $K_\phi$  that gives a flux function of the form  $\psi_d \propto \text{constant} - r^2$  or  $\psi_d \propto \text{constant}$ .

To begin with, we perform azimuthal integration in these equations. The integration can be written in terms of the Laplace coefficient known in celestial mechanics (see, e.g., Murray & Dermott 1999). The series expansion of the Laplace coefficient gives

$$\int_0^{2\pi} \frac{\cos \phi' d\phi'}{(r^2 + r'^2 - 2rr' \cos \phi')^{1/2}} = \frac{\pi}{r_>} \sum_{n=0}^{\infty} c_n \left( \frac{r_<}{r_>} \right)^{2n+1}, \quad (\text{B2})$$

$$c_n = \frac{\left(\frac{1}{2}\right)_n \left(\frac{3}{2}\right)_n}{(1)_n (2)_n}, \quad (\text{B3})$$

where  $(a)_n = a(a+1) \cdots (a+n-1)$  is the Pochhammer symbol. One can show, by using Equation (B2) together with the relations  $\sum_{n=0}^{\infty} c_n \alpha^{2n+1} = (4/\pi\alpha)[K(\alpha) - E(\alpha)]$  and  $rr'/r_< = r_>$ , that Equation (B1) is equivalent to Equation (12). Putting Equation (B2) into Equation (B1), we obtain Biot–Savart's equation after azimuthal integration,

$$\psi_d = \frac{\pi}{c} \sum_{n=0}^{\infty} c_n \left[ \frac{1}{r^{2n+1}} \int_{r_{\text{in}}}^r r'^{2n+2} K_\phi dr' + r^{2(n+1)} \int_r^{r_{\text{out}}} \frac{K_\phi dr'}{r'^{2n+1}} \right], \quad (\text{B4})$$

for  $r_{\text{in}} < r < r_{\text{out}}$ .

### B.1. Analogy with Inverse Problems for Gravitational Fields

Before we proceed, it is useful to see how our problem resembles inverse problems of axisymmetric *scalar* fields. As pointed out by LPP94a, solving Biot–Savart's equation for  $K_\phi$  is analogous to finding the surface density distribution of a disk for a given gravitational potential distribution. For example, for an axisymmetric disk with surface density profile  $\Sigma(r)$ , the gravitational potential  $\Phi(r)$  is given by

$$\Phi(r) = -G \int_{r_{\text{in}}}^{r_{\text{out}}} r' dr' \int_0^{2\pi} d\phi' \frac{\Sigma(r')}{(r^2 + r'^2 - 2rr' \cos \phi')^{1/2}}, \quad (\text{B5})$$

where  $G$  is the gravitational constant. Equation (B5) is identical to Equation (B1) if we replace  $G\Sigma(r') \rightarrow K_\phi(r') \cos \phi'$  and  $\Phi \rightarrow -c\psi_d/r$ . A similar equation can be found in the problem of finding the pressure distribution  $P(r)$  on the interface of two elastic spheres for given surface displacement distribution  $u_z(r)$ , in which case  $G\Sigma \rightarrow P$  and  $\Phi \rightarrow -\pi E^* u_z$ , where  $E^*$  is the reduced Young modulus (Johnson 1987; Landau & Lifshitz 1986).

It is known that Equation (B5) has two types of exact solutions in the limit of  $r_{\text{in}} \rightarrow 0$ . The first type is

$$\Sigma(r) = \left[ 1 - \left( \frac{r}{r_{\text{out}}} \right)^2 \right]^{1/2} \Sigma_c, \quad (\text{B6})$$

where  $\Sigma_c$  is a constant. Equation (B6) gives a harmonic gravitational potential

$$\Phi(r) = -\frac{\pi^2 G \Sigma_c r_{\text{out}}}{2} \left[ 1 - \frac{1}{2} \left( \frac{r}{r_{\text{out}}} \right)^2 \right]. \quad (\text{B7})$$

The second type is

$$\Sigma(r) = \left[ 1 - \left( \frac{r}{r_{\text{out}}} \right)^2 \right]^{-1/2} \Sigma_c, \quad (\text{B8})$$

where  $\Sigma_c$  is a constant. Equation (B8) gives a constant potential

$$\Phi = -\pi^2 G \Sigma_c r_{\text{out}}. \quad (\text{B9})$$

In contact mechanics ( $\Sigma \rightarrow P$  and  $\Phi/G \rightarrow -\pi E^* u_z$ ), the first and second types are known as Hertz's and Boussinesq's solutions, respectively (Johnson 1987; Landau & Lifshitz 1986). These solutions are useful when we guess the functional form of  $K_\phi$  for given  $\psi_d$ .

### B.2. Solution Near the Outer Boundary

We first solve Equation (B4) for  $\psi_d = \psi_{\text{in}} - B_\infty r^2/2$  (Equation (23)). In this subsection, we focus on how the solution behaves near the outer boundary ( $r \sim r_{\text{out}}$ ), and for this reason we will take  $r_{\text{in}}$  to be zero. As described in the main text, the asymptotic behavior of the solution  $r \ll r_{\text{out}}$  shows that the solution must be of the form  $K_\phi(r') = (c\psi_{\text{in}}/2\pi r'^2)f_{\text{out}}(r')$  (Equation (29)), where  $f_{\text{out}}$  satisfies  $f_{\text{out}} \rightarrow 1$  as  $r'/r_{\text{out}} \rightarrow 0$ .

To carry out the integration in Equation (B4), we expand  $f_{\text{out}}$  in powers of  $r'/r_{\text{out}}$ ,

$$f_{\text{out}}(r') = 1 + \sum_{m=0}^{\infty} a_{2m+1} \left( \frac{r'}{r_{\text{out}}} \right)^{2m+1}, \quad (\text{B10})$$

where  $a_{2m+1}$  ( $m = 0, 1, 2, \dots$ ) are constants, and we have used that  $f_{\text{out}} \rightarrow 1$  as  $r'/r_{\text{out}} \rightarrow 0$ . We have assumed that  $K_\phi$  does not involve terms  $r'^{2m}$  ( $m = 1, 2, \dots$ ) because such terms would yield unwanted logarithmic terms in the resultant  $\psi_d(r)$ .

With Equation (B10), the integration in Equation (B4) can be analytically performed. The result reads

$$\begin{aligned} \psi_d = & \frac{\psi_{\text{in}}}{2} \sum_{n=0}^{\infty} c_n \left[ \frac{1}{2(n+1)} + \frac{1}{2n+1} \right] \\ & + \frac{\psi_{\text{in}}}{2} \sum_{m=0}^{\infty} a_{2m+1} \left( \frac{r}{r_{\text{out}}} \right)^{2m+1} \\ & \times \sum_{n=0}^{\infty} c_n \left[ \frac{1}{2(n+m+1)} + \frac{1}{2(n-m)+1} \right] \\ & + \frac{\psi_{\text{in}}}{2} \sum_{n=0}^{\infty} c_n \left( \frac{r}{r_{\text{out}}} \right)^{2(n+1)} \left[ -\frac{1}{2(n+1)} + \sum_{m=0}^{\infty} \frac{a_{2m+1}}{2(m-n)-1} \right]. \end{aligned} \quad (\text{B11})$$

This result can be simplified if we use the relation

$$\begin{aligned} & \sum_{n=0}^{\infty} c_n \left[ \frac{1}{2(n+m+1)} + \frac{1}{2(n-m)+1} \right] \\ & = \frac{{}_3F_2\left(\frac{1}{2}, \frac{3}{2}, m+1; 2, m+2; 1\right)}{2(m+1)} + \frac{{}_3F_2\left(\frac{1}{2}, \frac{3}{2}, \frac{1-2m}{2}; 2, \frac{3-2m}{2}; 1\right)}{1-2m} \\ & = \begin{cases} 2, & m=0, \\ 0, & m=1, 2, \dots \end{cases} \end{aligned} \quad (\text{B12})$$

(one can verify this with *Mathematica*). With this relation, we obtain

$$\psi_d = \psi_{\text{in}} + \frac{\psi_{\text{in}} a_1 r}{r_{\text{out}}}$$

$$+ \frac{\psi_{\text{in}}}{2} \sum_{n=0}^{\infty} c_n \left( \frac{r}{r_{\text{out}}} \right)^{2(n+1)} \left[ -\frac{1}{2(n+1)} + \sum_{m=0}^{\infty} \frac{a_{2m+1}}{2(m-n)-1} \right]. \quad (\text{B13})$$

Comparing this with  $\psi_d = \psi_{\text{in}} - B_\infty r^2/2$ , we find that the second term of Equation (B13) must vanish, and that the infinite sum in the third term must leave a term proportional to  $r^2$ . Hence, the coefficients  $a_1, a_3, a_5, \dots$  must satisfy the relations

$$a_1 = 0, \quad (\text{B14})$$

$$\sum_{m=1}^{\infty} \frac{a_{2m+1}}{2(m-n)-1} = \frac{1}{2(n+1)} \quad n = 1, 2, \dots \quad (\text{B15})$$

Unfortunately, we could not find the set of  $a_{2m+1}$  that exactly satisfies Equation (B15). However, an approximate but fully accurate solution can be obtained if we note that the flux function under consideration is of the same functional form as the harmonic gravitational potential (Equation (B7)). By analogy with Equation (B6), let us consider the following ansatz for  $f_{\text{out}}$ ,

$$f_{\text{out}}(r') = 1 + \frac{r'}{r_{\text{out}}} \left\{ \left[ 1 - \left( \frac{r'}{r_{\text{out}}} \right)^2 \right]^\gamma - 1 \right\}, \quad (\text{B16})$$

where  $\gamma$  is a fitting parameter to be determined below. We may assume  $\gamma > -1$  since otherwise the radially integrated current  $2\pi \int_0^{r_{\text{out}}} K_\phi(r') r' dr'$  would diverge. The ansatz is equivalent to Equation (B10) with  $a_1 = 0$  and

$$a_{2m+1} = \frac{(-1)^m}{m!} \frac{\Gamma(\gamma+1)}{\Gamma(\gamma+1-m)}, \quad m = 1, 2, \dots \quad (\text{B17})$$

This ansatz is useful because the infinite sum  $\sum_{m=1}^{\infty} \frac{a_{2m+1}}{2(m-n)-1}$  has a closed expression

$$\sum_{m=1}^{\infty} \frac{a_{2m+1}}{2(m-n)-1} = \frac{1}{1+2n} + \frac{\Gamma(-\frac{1}{2}-n)\Gamma(1+\gamma)}{2\Gamma(\frac{1}{2}-n+\gamma)}. \quad (\text{B18})$$

By a least-squares method, we find that the right-hand side of Equation (B18) best approximates that of Equation (B15) when  $\gamma = 0.43$  (Figure 9).

In the main text we have introduced  $\psi_{\text{in}}$  as an undetermined quantity. As we will see below, this quantity is determined as an *eigenvalue* of the inversion problem under consideration. Substitution of Equations (B14) and (B15) into Equation (B13) shows that  $\psi_d$  must be of the form

$$\psi_d = \psi_{\text{in}} + \frac{\psi_{\text{in}}}{2} \left( -\frac{1}{2} + \sum_{m=0}^{\infty} \frac{a_{2m+1}}{2m-1} \right) \left( \frac{r}{r_{\text{out}}} \right)^2, \quad (\text{B19})$$

where we have used that  $c_0 = 1$ . The infinite sum remaining in the above equation can be evaluated as  $\sum_{m=1}^{\infty} \frac{a_{2m+1}}{2m-1} \approx -0.502 \approx -1/2$  if we use Equation (B18) with the best-fit  $\gamma = 0.43$  (see also Figure 9). Thus, we find

$$\psi_d = \psi_{\text{in}} \left[ 1 - \frac{1}{2} \left( \frac{r}{r_{\text{out}}} \right)^2 \right]. \quad (\text{B20})$$

Imposing that this is equal to  $\psi_{\text{in}} - B_\infty r^2/2$ , we obtain  $\psi_{\text{in}} = B_\infty r_{\text{out}}^2$ .

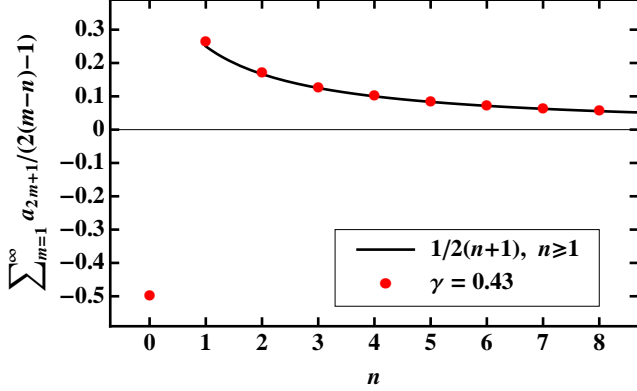


**Figure 9.** Values of  $\sum_{m=1}^{\infty} \frac{a_{2m+1}}{2(m-n)-1}$  ( $n = 0, 1, 2, \dots$ ) for  $\gamma = 0.43$  (circles) from Equation (B18). The curve indicates the right-hand side of Equation (B15).

### B.3. Solution Near the Inner Boundary

Next we show how  $K_\phi$  behaves near the inner boundary  $r \sim r_{\text{in}}$ . We take  $r_{\text{out}}$  to be infinitely large and approximate  $\psi_d$  with a constant  $\psi_{\text{in}}$ . As we did for the outer boundary, we assume the solution of the form  $K_\phi(r') = (c\psi_{\text{in}}/2\pi r'^2)f_{\text{in}}(r')$ , where  $f_{\text{in}}$  approaches unity as  $r'/r_{\text{in}} \rightarrow \infty$ .

Let us expand  $f_{\text{out}}$  as

$$f_{\text{in}}(r') = 1 + \sum_{m=1}^{\infty} b_{2m} \left( \frac{r'}{r_{\text{in}}} \right)^{-2m}, \quad (\text{B21})$$

where  $b_{2m}$  ( $m = 1, 2, \dots$ ) are constants. We have assumed that  $f_{\text{in}}$  is an even function of  $r'$  because otherwise the resulting  $\psi_d(r)$  would involve unwanted logarithmic terms. Substituting Equation (B21) into Equation (B4), performing integration, and using Equation (B12), we obtain

$$\psi_d = \psi_{\text{in}} + \frac{\psi_{\text{in}}}{2} \sum_{n=0}^{\infty} c_n \left( \frac{r_{\text{in}}}{r} \right)^{2n+1} \left[ -\frac{1}{2n+1} + \sum_{m=1}^{\infty} \frac{b_{2m}}{2(m-n)-1} \right]. \quad (\text{B22})$$

Since this must be equal to  $\psi_{\text{in}}$ ,  $b_{2m}$  ( $m = 1, 2, \dots$ ) must satisfy the relation

$$\sum_{m=1}^{\infty} \frac{b_{2m}}{2(m-n)-1} = \frac{1}{2n+1}, \quad n = 0, 1, \dots \quad (\text{B23})$$

Now let us consider the ansatz

$$f_{\text{in}}(r) = \left[ 1 - \left( \frac{r'}{r_{\text{in}}} \right)^{-2} \right]^{-\kappa}, \quad (\text{B24})$$

where  $\kappa$  is a constant (see Equation (B8)). We require  $\kappa < 1$  in order for the radially integrated surface current to be finite. Equation (B24) is equivalent to Equation (B21) with

$$b_{2m} = \frac{(-1)^m}{m!} \frac{\Gamma(1-\kappa)}{\Gamma(1-m-\kappa)}, \quad m = 1, 2, \dots \quad (\text{B25})$$

It can be shown that  $b_{2m}$  given by Equation (B25) satisfies

$$\sum_{m=1}^{\infty} \frac{b_{2m}}{2(m-n)-1} = \frac{1}{2n+1} + \frac{\Gamma(-\frac{1}{2}-n)\Gamma(\kappa-1)}{2\Gamma(\frac{1}{2}-n-\kappa)}. \quad (\text{B26})$$

The poles of  $\Gamma(\frac{1}{2}-n-\kappa)$  suggest that Equation (B23) holds for all  $n (= 0, 1, 2, \dots)$  when  $\kappa = 1/2, 3/2, 5/2, \dots$ . Among

them, only  $\kappa = 1/2$  is the physical solution since the others do not satisfy  $\kappa < 1$ . Thus, we find that  $f_{\text{in}}$  is exactly given by Equation (B24) with  $\kappa = 1/2$ .

### C. DISK-INDUCED FLUX IN REGIONS I AND III

Here we derive full analytic expressions for the disk-induced flux  $\psi_d$  and corresponding field strength  $B_{z,d}$  in regions I and III. From the definition of the flux function (Equation (2)), the disk-induced field strength is given by

$$B_{z,d} = \frac{1}{r} \frac{\partial \psi_d}{\partial r}. \quad (\text{C1})$$

#### C.1. Region I

As we did in Appendix B, we perform the integration in Equation (41) by expanding the kernel  $R(r, r')$  in powers of  $r/r'$ . Applying Equations (B1) and (B2) to region I where  $r < r_{\text{in}} < r'$ , we obtain an equation similar to Equation (B4),

$$\psi_{d,I} = \frac{\pi}{c} \sum_{n=0}^{\infty} c_n r^{2(n+1)} \int_{r_{\text{in}}}^{r_{\text{out}}} \frac{K_\phi(r')}{r'^{2n+1}} dr'. \quad (\text{C2})$$

Below we will assume  $r_{\text{out}} \rightarrow \infty$  since the contribution of the outer boundary to  $\psi_{d,I}$  is small.

Inserting the current density given by Equation (39) into the above equation and neglecting the correction factor  $f_{\text{out}}$  for the outer boundary, we have

$$\psi_{d,I} = \frac{1}{2} B_\infty r_{\text{out}}^2 \sum_{n=0}^{\infty} c_n r^{2(n+1)} \int_{r_{\text{in}}}^{\infty} \frac{f_{\text{in}}(r')}{r'^{2n+3}} dr', \quad (\text{C3})$$

where the correction factor  $f_{\text{in}}$  for the inner boundary is given by Equation (38). The integral can be reduced, by introducing a variable  $x = (r_{\text{in}}/r)^2$ , to

$$\int_{r_{\text{in}}}^{\infty} \frac{f_{\text{in}}(r')}{r'^{2n+3}} dr' = \int_0^1 \frac{x^n (1-x)^{-1/2} dx}{2r_{\text{in}}^{2(n+1)}} = \frac{B(n+1, \frac{1}{2})}{2r_{\text{in}}^{2(n+1)}}, \quad (\text{C4})$$

where  $B(x, y)$  is the Beta function. It can also be shown with *Mathematica* that

$$\sum_{n=0}^{\infty} c_n B(n+1, \frac{1}{2}) \left( \frac{r}{r_{\text{in}}} \right)^{2(n+1)} = 4 - 4 \sqrt{1 - \left( \frac{r}{r_{\text{in}}} \right)^2}. \quad (\text{C5})$$

Using these relations, we finally obtain

$$\psi_{d,I} = B_\infty r_{\text{out}}^2 \left[ 1 - \sqrt{1 - \left( \frac{r}{r_{\text{in}}} \right)^2} \right]. \quad (\text{C6})$$

From Equation (C1), we also obtain the strength of the induced vertical field,

$$B_{z,d,I} = \left( \frac{r_{\text{out}}}{r_{\text{in}}} \right)^2 \frac{B_\infty}{\sqrt{1 - (r/r_{\text{in}})^2}}. \quad (\text{C7})$$

Note that  $B_{z,I} \gg B_\infty$  and hence  $B_z \approx B_{z,d,I}$ . In the limit of  $r \ll r_{\text{in}}$ , Equations (C6) and (C7) reduce to Equations (43) and (44) in the main text, respectively.

#### C.2. Region III

Similarly, we perform the integration in Equation (42) by expanding  $R(r', r)$  using Equations (B1) and (B2). Noting that

$r' < r_{\text{out}} < r$  for region III, we obtain

$$\psi_{d,I} = \frac{\pi}{c} \sum_{n=0}^{\infty} c_n r^{-(2n+1)} \int_{r_{\text{in}}}^{r_{\text{out}}} r'^{2(n+1)} K_\phi(r') dr'. \quad (\text{C8})$$

Below we will assume  $r_{\text{in}} \rightarrow 0$  and neglect the contribution of the inner boundary to  $\psi_{d,III}$ .

Inserting Equation (39) into the above equation and neglecting the inner correction factor  $f_{\text{in}}$ , we have

$$\psi_{d,III} = \frac{1}{2} B_\infty r_{\text{out}}^2 \sum_{n=0}^{\infty} c_n r^{-(2n+1)} \int_0^{r_{\text{out}}} r'^{2n} f_{\text{out}}(r') dr', \quad (\text{C9})$$

where  $f_{\text{out}}$  is given by Equation (33). By introducing a variable  $y = (r/r_{\text{out}})^2$ , the integration can be performed as

$$\begin{aligned} & \int_0^{r_{\text{out}}} r'^{2n} f_{\text{out}}(r') dr' \\ &= \frac{r_{\text{out}}^{2n+1}}{2} \int_0^1 \left[ y^{n-\frac{1}{2}} - y^n + y^n (1-y)^\gamma \right] dy \\ &= \frac{r_{\text{out}}^{2n+1}}{2} \left[ \frac{1}{1+3n+2n^2} + B(1+n, 1+\gamma) \right], \quad (\text{C10}) \end{aligned}$$

where  $B(x, y)$  is again the Beta function. It can then be shown with *Mathematica* that

$$\begin{aligned} & \sum_{n=0}^{\infty} c_n \left[ \frac{1}{1+3n+2n^2} + B(1+n, 1+\gamma) \right] \left( \frac{r_{\text{out}}}{r} \right)^{2(n+1)} \\ &= \frac{2r}{r_{\text{out}}} \left[ F\left(-\frac{1}{2}, -\frac{1}{2}, 1, \frac{r_{\text{out}}^2}{r^2}\right) - F\left(-\frac{1}{2}, \frac{1}{2}, 1+\gamma, \frac{r_{\text{out}}^2}{r^2}\right) \right], \quad (\text{C11}) \end{aligned}$$

where  $F(a, b, c; z)$  is the hypergeometric function. Using these relations,  $\psi_{d,III}$  can be written as

$$\psi_{d,III} = \frac{B_\infty r r_{\text{out}}}{2} \left[ F\left(-\frac{1}{2}, -\frac{1}{2}, 1, \frac{r_{\text{out}}^2}{r^2}\right) - F\left(-\frac{1}{2}, \frac{1}{2}, 1+\gamma, \frac{r_{\text{out}}^2}{r^2}\right) \right], \quad (\text{C12})$$

and from Equation (C1), we also obtain the induced vertical field

$$B_{z,d,III} = \frac{r_{\text{out}}}{r} \left[ \frac{2}{\pi} E\left(\frac{r_{\text{out}}^2}{r^2}\right) - F\left(\frac{1}{2}, \frac{1}{2}, 1+\gamma, \frac{r_{\text{out}}^2}{r^2}\right) \right]. \quad (\text{C13})$$

The asymptotic form of  $\psi_{d,II}$  at  $r \gg r_{\text{out}}$  can be easily obtained by dropping the  $n \geq 1$  terms in Equation (C9), namely,

$$\begin{aligned} \psi_{d,III} &\approx \frac{B_\infty r_{\text{out}}^2}{2r} \int_0^{r_{\text{out}}} f_{\text{out}}(r') dr' \\ &\approx \frac{B_\infty r_{\text{out}}^3}{4r} [1 + B(1, 1+\gamma)] \approx 0.425 \frac{B_\infty r_{\text{out}}^3}{r}, \quad (\text{C14}) \end{aligned}$$

where we have used that Equation (C10),  $c_0 = 1$ , and  $B(1, 1+\gamma) \approx 0.7$  for the best-fit parameter  $\gamma = 0.43$  (see Appendix B.2). The corresponding  $B_z$  is

$$B_{z,d,III} \approx -0.425 \left( \frac{B_\infty r_{\text{out}}}{r} \right)^3. \quad (\text{C15})$$

## REFERENCES

- Agapitou, V., & Papaloizou, J. C. B. 1996, *ApL&C*, 34, 363  
 Allen, A., Shu, F. H., & Li, Z.-Y. 2003, *ApJ*, 599, 351  
 Andrews, S. M., Wilner, D. J., Hughes, A. M., Qi, C., & Dullemond, C. P. 2009, *ApJ*, 700, 1502  
 Armitage, P. J., Simon, J. B., & Martin, R. G. 2013, *ApJL*, 778, L14  
 Bai, X.-N. 2011, *ApJ*, 739, 50  
 Bai, X.-N. 2013, *ApJ*, 772, 96  
 Bai, X.-N. 2014, *ApJ*, submitted (arXiv:1402.7102)  
 Bai, X.-N., & Stone, J. M. 2013a, *ApJ*, 767, 30  
 Bai, X.-N., & Stone, J. M. 2013b, *ApJ*, 769, 76  
 Balbus, S. A., & Hawley, J. F. 1991, *ApJ*, 376, 214  
 Balbus, S. A., & Hawley, J. F. 1998, *RvMP*, 70, 1  
 Beckwith, K., Hawley, J. F., & Krolik, J. H. 2009, *ApJ*, 707, 428  
 Bisnovaty-Kogan, G. S., & Lovelace, R. V. E. 2007, *ApJL*, 667, L167  
 Bisnovaty-Kogan, G. S., & Lovelace, R. V. E., 2012, *ApJ*, 750, 109  
 Bisnovaty-Kogan, G. S., & Ruzmaikin, A. A., 1974, *Ap&SS*, 28, 45  
 Blandford, R. D., & Payne, D. G. 1982, *MNRAS*, 199, 883  
 Braithwaite, J. 2012, *MNRAS*, 422, 619  
 Brandenburg, A., Nordlund, A., Stein, R. F., & Torkelsson, U. 1995, *ApJ*, 446, 741  
 Calvet, N., Muzerolle, J., Briceño, C., et al. 2004, *AJ*, 128, 1294  
 Cao, X., & Spruit, H. C. 2002, *A&A*, 385, 289  
 Carballido, A., Stone, J. M., & Pringle, J. E. 2005, *MNRAS*, 358, 1055  
 Crutcher, R. M., Hakobian, N., & Troland, T. H. 2009, *ApJ*, 692, 844  
 Dapp, W. B., Basu, S., & Kunz, M. W. 2012, *A&A*, 541, A35  
 Davis, S. W., Stone, J. M., & Pessah, M. E. 2010, *ApJ*, 713, 52  
 Dzyurkevich, N., Turner, N. J., Henning, T., & Kley, W. 2013, *ApJ*, 765, 114  
 Flock, M., Dzyurkevich, N., Klahr, H., Turner, N., & Henning, T. 2012a, *ApJ*, 744, 144  
 Flock, M., Henning, T., & Klahr, H. 2012b, *ApJ*, 761, 95  
 Fromang, S., & Papaloizou, J. 2006, *A&A*, 452, 751  
 Fromang, S., & Stone, J. M. 2009, *A&A*, 507, 19  
 Galli, D., Lizano, S., Shu, F. H., & Allen, A. 2006, *ApJ*, 647, 374  
 Galli, D., & Shu, F. H. 1993, *ApJ*, 417, 220  
 Gressel, O. 2010, *MNRAS*, 405, 41  
 Gressel, O., Nelson, R. P., & Turner, N. J. 2011, *MNRAS*, 415, 3291  
 Gressel, O., Nelson, R. P., & Turner, N. J. 2012, *MNRAS*, 422, 1240  
 Guan, X., & Gammie, C. F. 2009, *ApJ*, 697, 1901  
 Guilet, J., & Ogilvie, G. I. 2012, *MNRAS*, 424, 2097  
 Guilet, J., & Ogilvie, G. I. 2013, *MNRAS*, 430, 822  
 Guilet, J., & Ogilvie, G. I. 2014, *MNRAS*, in press (arXiv:1403.3732)  
 Hartmann, L., Calvet, N., Gullbring, E., & D'Alessio, P. 1998, *ApJ*, 495, 385  
 Hawley, J. F., Gammie, C. F., & Balbus, S. A. 1995, *ApJ*, 440, 742  
 Hayashi, C. 1981, *PTPhS*, 70, 35  
 Igumenshchev, I. V., Narayan, R., & Abramowicz, M. A. 2003, *ApJ*, 592, 1042  
 Jackson, J. D. 1998, *Classical Electrodynamics* (3rd ed.; New York: Wiley)  
 Johansen, A., Klahr, H., & Mee, A. J. 2006, *MNRAS*, 370, L71  
 Johns-Krull, C. M. 2007, *ApJ*, 664, 975  
 Johnson, K. L. 1987, *Contact Mechanics* (Cambridge: Cambridge Univ. Press)  
 Kitamura, Y., Momose, M., Yokogawa, S., et al. 2002, *ApJ*, 581, 357  
 Kunz, M. W., & Lesur, G. 2013, *MNRAS*, 434, 2295  
 Landau, L. D., & Lifshitz, E. M. 1986, *Theory of Elasticity* (3rd ed; Oxford: Butterworth-Heinemann)  
 Laughlin, G., Steinacker, A., & Adams, F. C. 2004, *ApJ*, 608, 489  
 Lesur, G., & Longaretti, P.-Y. 2009, *A&A*, 504, 309  
 Li, Z.-Y., & Shu, F. H. 1997, *ApJ*, 475, 237  
 Lovelace, R. V. E. 1976, *Natur*, 262, 649  
 Lovelace, R. V. E., Rothstein, D. M., & Bisnovaty-Kogan, G. S. 2009, *ApJ*, 701, 885  
 Lubow, S. H., Papaloizou, J. C. B., & Pringle, J. E. 1994a, *MNRAS*, 267, 235 (LPP94a)  
 Lubow, S. H., Papaloizou, J. C. B., & Pringle, J. E. 1994b, *MNRAS*, 268, 1010  
 Machida, M. N., Inutsuka, S., & Matsumoto, T. 2007, *ApJ*, 670, 1198  
 Moll, R. 2012, *A&A*, 548, A76  
 Murray, C. D., & Dermott, S. F. 1999, *Solar System Dynamics* (Cambridge: Cambridge Univ. Press)  
 Nakano, T. 1984, *FCPh*, 9, 139  
 Nakano, T., Nishi, R., & Umebayashi, T. 2002, *ApJ*, 573, 199  
 Nelson, R. P. 2005, *A&A*, 443, 1067  
 Nelson, R. P., & Papaloizou, J. C. B. 2004, *MNRAS*, 350, 849  
 Ogilvie, G. I. 1997, *MNRAS*, 288, 63  
 Ogilvie, G. I., & Livio, M. 2001, *ApJ*, 553, 158  
 Okuzumi, S., & Hirose, S. 2011, *ApJ*, 742, 65  
 Okuzumi, S., & Hirose, S. 2012, *ApJL*, 753, L8  
 Okuzumi, S., & Ormel, C. W. 2013, *ApJ*, 771, 43  
 Ormel, C. W., & Okuzumi, S. 2013, *ApJ*, 771, 44  
 Pessah, M. E., Chan, C.-K., & Psaltis, D. 2007, *ApJL*, 668, L51  
 Rothstein, D. M., & Lovelace, R. V. E. 2008, *ApJ*, 677, 1221  
 Sano, T., Inutsuka, S., Turner, N. J., & Stone, J. M. 2004, *ApJ*, 605, 321  
 Shu, F., Najita, J., Ostriker, E., et al. 1994, *ApJ*, 429, 781  
 Shu, F. H., Galli, D., Lizano, S., & Cai, M. 2006, *ApJ*, 647, 382  
 Sicilia-Aguilar, A., Hartmann, L. W., Hernández, J., Briceño, C., & Calvet, N. 2005, *AJ*, 130, 188  
 Simon, J. B., Bai, X.-N., Stone, J. M., Armitage, P. J., & Beckwith, K. 2013a, *ApJ*, 764, 66  
 Simon, J. B., Bai, X.-N., Stone, J. M., Armitage, P. J., & Beckwith, K. 2013b, *ApJ*, 775, 73  
 Simon, J. B., Hawley, J. F., & Beckwith, K. 2011, *ApJ*, 730, 94

- Spruit, H. C. 1996, in *Evolutionary Processes in Binary Stars*, ed. R. A. M. J. Wijers, M. B. Davies, & C. A. Tout (NATO ASI Ser. C, 477; Dordrecht: Kluwer), 249
- Spruit H. C., & Uzdensky D. A. 2005, *ApJ*, 629, 960
- Suzuki, T. K., & Inutsuka, S. 2014, *ApJ*, 784, 121
- Suzuki, T. K., Muto, T., & Inutsuka, S. 2010, *ApJ*, 718, 1289
- Takeuchi, T., & Lin, D. N. C. 2002, *ApJ*, 81, 1344
- Takeuchi, T., & Okuzumi, S. 2014, *ApJ*, submitted (arXiv:1310.7380; Paper II)
- Tchekhovskoy, A., Narayan, R., & McKinney, J. C. 2011, *MNRAS*, 418, L79
- Troland, T. H., & Crutcher, R. M. 2008, *ApJ*, 680, 457
- Turner, N. J., & Sano, T. 2008, *ApJL*, 679, L131
- Turner, N. J., Willacy, K., Bryden, G., & Yorke, H. W. 2006, *ApJ*, 639, 1218
- van Ballegooijen, A. A. 1989, in *Accretion Disks and Magnetic Fields in Astrophysics*, ed. G. Belvedere (Astrophysics and Space Science Library, Vol. 156; Dordrecht: Kluwer), 99
- Wardle, M., 2007, *Ap&SS*, 311, 35
- Wardle, M., & Salmeron, R. 2012, *MNRAS*, 422, 2737
- Yang, C.-C., Mac Low, M.-M., & Menou, K. 2009, *ApJ*, 707, 1233
- Yang, C.-C., Mac Low, M.-M., & Menou, K. 2012, *ApJ*, 748, 79